AD-A157 445 NEUTRAL BEAM INTERACTIONS WITH MATERIALS(U) MICHIGAN 1/1
UNIV ANN ARBOR COLL OF ENGINEERING
R M GILGENBACH ET AL. 18 JUN 85 AFOSR-84-0130
UNCLASSIFIED F/G 20/8 NL

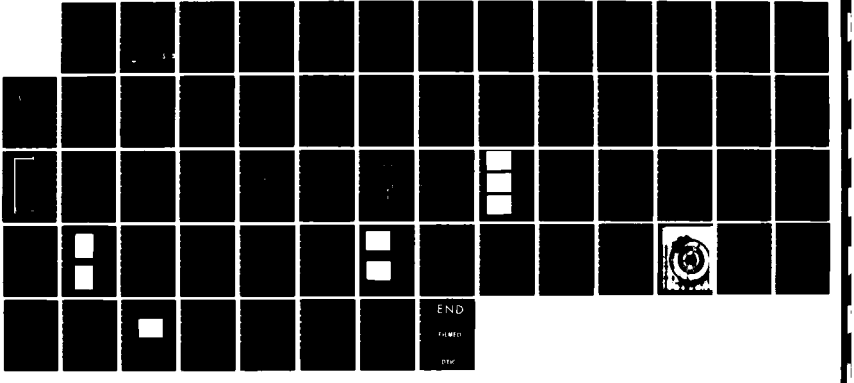

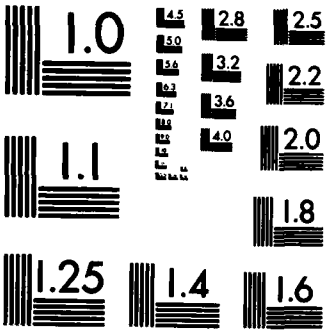

(2)

Annual Progress Report to:
The Air Force Office of Scientific Research
for the Project:

Neutral Beam Interactions with Materials (AFOSR 84-0130)

R.M. Gilgenbach
Nuclear Engineering Dept.

J. J. Duderstadt
Nuclear Eng. Dept. and
Dean, College of Engineering

R.S. Ong
Aerospace Eng. Dept.

June 1985

Intense Energy Beam Interaction Laboratory

UNCLASSIFIED

SECURITY CLASSIFICATION OF THIS PAGE

AD A157 445

REPORT DOCUMENTATION PAGE

1a. REPORT SECURITY CLASSIFICATION: Unclassified	1b. RESTRICTIVE MARKINGS
2a. SECURITY CLASSIFICATION AUTHORITY	3. DISTRIBUTION/AVAILABILITY OF REPORT: Unclassified, approved for public release, distribution unlimited
2b. DECLASSIFICATION/DOWNGRADING SCHEDULE	
4. PERFORMING ORGANIZATION REPORT NUMBER(S): AFOSR84-0130	5. MONITORING ORGANIZATION REPORT NUMBER(S)
6a. NAME OF PERFORMING ORGANIZATION: University of Michigan; 6b. OFFICE SYMBOL (If applicable)	7a. NAME OF MONITORING ORGANIZATION: Air Force Office of Scientific Research
6c. ADDRESS (City, State and ZIP Code): Nuclear Engineering Department, Ann Arbor, MI 48109	7b. ADDRESS (City, State and ZIP Code): Physical and Geophysical Sciences, Bolling Air Force Base, Washington, DC
8a. NAME OF FUNDING/SPONSORING ORGANIZATION: AFOSR; 8b. OFFICE SYMBOL (If applicable)	9. PROCUREMENT INSTRUMENT IDENTIFICATION NUMBER: AFOSR84-0130
8c. ADDRESS (City, State and ZIP Code): Physical and Geophysical Sciences, Bolling AFB, Washington, DC	10. SOURCE OF FUNDING NOS. — PROGRAM ELEMENT NO. / PROJECT NO. / TASK NO. / WORK UNIT NO.
11. TITLE (Include Security Classification): Annual Report. Neutral Beam Interactions with Mtrls.	
12. PERSONAL AUTHOR(S): R. M. Gilgenbach and J. J. Duderstadt	
13a. TYPE OF REPORT: Annual; 13b. TIME COVERED: FROM 6/1/84 TO 5/31/85	14. DATE OF REPORT (Yr., Mo., Day): June 18, 1985; 15. PAGE COUNT: 58
16. SUPPLEMENTARY NOTATION	
17. COSATI CODES — FIELD / GROUP / SUB. GR.	18. SUBJECT TERMS (Continue on reverse if necessary and identify by block number): Neutral beams, radiation signatures, and beam-material interactions.

19. ABSTRACT (Continue on reverse if necessary and identify by block number)

Abstract

This annual report describes experimental and theoretical research which concerns the interaction of neutral or ion beams with surface ablation plasmas. This problem is of interest in the case of particle penetration to outgassing or ablating objects in a high vacuum environment. We have constructed a neutral beam-ablation plasma experiment which employs a Q-switched ruby laser to independently generate a dense ablation plasma.

Expand to include 1

(continued other side)

20. DISTRIBUTION/AVAILABILITY OF ABSTRACT: UNCLASSIFIED/UNLIMITED ☒ SAME AS RPT. ☐ DTIC USERS ☐	21. ABSTRACT SECURITY CLASSIFICATION: Unclassified
22a. NAME OF RESPONSIBLE INDIVIDUAL: Dr. Robert Barker	22b. TELEPHONE NUMBER (Include Area Code): (202) 767-5011; 22c. OFFICE SYMBOL

DD FORM 1473, 83 APR — EDITION OF 1 JAN 73 IS OBSOLETE.

UNCLASSIFIED

The neutral beam is generated by a (5-20 keV) duopigatron ion source with charge exchange neutralization cell. Experimental results of beam attenuation show excellent agreement with predictions based on available cross-section data. In studying the attenuation of the neutral beams we have considered primarily charge exchange processes although we are estimating the relative contributions of momentum scattering and impact ionization. Line density values from a self-similar expansion model show good agreement with attenuation data. Spectroscopic measurements of the ablation plasma yield singly and doubly ionized lines.

We have developed a one-dimensional computational physics code which simulates the ablation of a carbon target by a proton beam. This is accomplished by coupling a sophisticated collisional-radiative equilibrium (CRE) ionization dynamics model, a one-dimensional, single temperature and fluid hydrodynamics model, and an energy deposition model. The total package is then applied to simulating the beam-target interaction under a variety of beam conditions. Other applications considered include heating due to inner-shell photon absorption and calculation of the amount of K_α radiation emitted by the direct interaction of a beam proton with a target atom.

The basic approach involves coupling a one-dimensional hydrodynamic code to an ionization dynamics and an energy deposition model. Because the radiation emitted by the plasma is an important diagnostic tool, we have tried to model the ionization dynamics very carefully. This is accomplished by developing an ionization dynamics model which considers a large number of excited states and atomic processes.

The atomic processes which are considered in our model are:

1) collisional ionization
2) three body recombination
3) collisional excitation
4) collisional de-excitation
5) spontaneous emission
6) radiative recombination
7) dielectric recombination.

We have developed a model for structured low Z projectile ions (those carrying electrons) in cold (neutral) or ionized targets in the local plasma approximation. Special attention has been paid to shell corrections which are likely to be important in the energy regime of interest. Corrections to first Born calculations include polarization and Bloch terms.

Annual Progress Report to:

The Air Force Office of Scientific Research

for the Project:

"Neutral Beam Interactions with Materials"

AFOSR84-0130

R. M. Gilgenbach, J. J. Duderstadt, R. S. Ong

Nuclear Engineering Department

The University of Michigan

Ann Arbor, Michigan 48109

June 1985

CONTENTS

Introduction

During the past year we have performed experimental and theoretical research regarding the interaction of neutral beams with independently generated ablation plasmas. Some of the results included in this annual report were given in the 6 month interim report. We have, however, presented significant new data obtained during the second six months of this project.

I. Theoretical Progress

Ia. Stopping Power of Low-Z "Structured" Projectile Ions

We have developed a model to calculate the stopping power of low Z "structured" projectile ions (those with bound electrons) in the local plasma approximation[1] (LPA). The LPA averages a constant density free-electron stopping power expression over the target electron cloud. The projectile structure is accounted for through the screening effect of the bound electron distribution[2]. Binding effects are introduced by comparing the high-velocity result with a Bethe-like formula for partially ionized projectiles.

This formula is given by Kim and Cheng[3]. We ignore losses due to projectile excitation and extend the result to the next order term by the technique of Fano and Turner[4] in order to be able to account for shell effects. The agreement with the LPA is very good provided the Lindhard-Scharff binding parameter[5] is introduced.

Shell effects are likely to be important in the energy

regime where projectiles can carry bound electrons into the target. For the bare ion case, in order to obtain agreement between theory[1] and experiment[6], it had been necessary to include the polarization ("Z3") and Bloch ("Z4") corrections. For low Z projectiles, these contributions tend to cancel. Hence, the modeling here will not be as detailed.

Deutsch[7] has given a compact formula for the polarization effect for bare ions. Since this contribution arises from distant collisions, we simply replace the projectile nuclear charge with its net charge.

The Bloch[8] correction arises from close collisions. Hence, it is tempting to leave the projectile nuclear charge alone, but this significantly overestimates the magnitude. Surprisingly, plausible results have been obtained by replacing the nuclear charge with the net charge[9] though the soundness of such an approach has been questioned[10]. We continue to search for the proper way to reduce this correction due to the screening of the projectile.

Target Ionization:

As the target becomes ionized, free electrons contribute to the stopping power. This may be calculated from our high-velocity expansion for bound electrons by replacing the Fermi distribution for a degenerate gas with a Fermi-Dirac distribution of a nondegenerate gas with finite temperature. This was possible by applying the expansion technique of Sigmund and Fu[11] to structured projectiles. For the special case of bare ions, our

result agrees with a temperature dependent calculation of Deutsch[12].

The remaining bound electrons will be reduced in number and more tightly bound than the original neutral target electrons. This is partially accounted for in the LPA by using appropriate wave functions[13] to describe the target ion electron distribution. The increased binding enters through the Lindhard-Scharff binding parameter (LSBP).

Peek[14] was the first to recognize that the LSBP must scale with the degree of target ionization in order to agree with more detailed first Born calculations[15]. This scaling was wholly empirical in nature. Without it, the LPA was thought to break down for ionized targets. The original arguments[5] gave the LSBP a constant value. However, these arguments were based on a Thomas-Fermi (many-electron) picture of the atom, clearly not suitable for, say, a one-electron ion. We have demonstrated that the appropriate scaling of the LSBP is observed when the Lindhard-Scharff argument[5] is repeated for a one-electron ion. Thus, the soundness of the LPA is strengthened. This affects both the "Z2" and the "Z3" stopping, both described by the LPA.

The Bloch[8] correction will also be affected by the increased binding since fewer collisions are likely to be close encounters. However, the usual form of this term does not readily suggest ways to incorporate this effect. Modeling the Bloch correction in terms of the LPA is presently being pursued.

I b.COMPUTER SIMULATION OF ION BEAM TARGET DYNAMICS AND RADIATION EMISSION

We have developed a one dimensional computational physics code which simulates the ablation of a carbon target by a proton beam. This is accomplished by coupling a sophisticated collisional-radiative equilibrium (CRE) ionization dynamics model, a one dimensional, single temperature and fluid hydrodynamics model, and an energy deposition model. The total package is then applied to simulating the beam-target interaction under a variety of initial beam conditions. Other applications considered include heating due to inner-shell photon absorption and calculation of the amount of K_α radiation emitted by the direct interaction of a beam proton with a target atom.

The basic approach involves coupling a one dimensional hydrodynamic codel to an ionization dynamics and an energy deposition model. Because the radiation emitted by the plasma is an important diagnostic tool, we have tried to model the ionization dynamics very carefully. This is accomplished by developing an ionization dynamics model which considers a large number of excited states and atomic processes.

The atomic processes which are considered in our model are:

1) collisional ionization
2) three body recombination
3) collisional excitation
4) collisional de-excitation
5) spontaneous emission

6) radiative recombination

7) dielectric recombination

These are incorporated into a set of rate equations which have the form[2]:

$$\frac{N(Z,j)}{dt} = [N_e N(Z-1,j'')S(Z-1,j'':Z,j) + N_e N(Z+1,j')$$

$$[\alpha(Z+1,j':Z,j) + N_e\beta(Z+1,j':Z,j)] +$$

$$\sum_{i>j} N(Z,i)A(i,j) + N_e \sum_{i>j} N(Z,i)X^{-1}(i,j) +$$

$$N_e \sum_{i>j} N(Z,i)X(i,j)]$$

$$-N(Z,j)[N_e S(Z,j:Z+1,j') + N_e[\alpha(Z,j:Z-1,j'') +$$

$$N_e\beta(Z,j:Z-1,j'')] + \sum_{i>j} A(j,i) +$$

$$N_e \sum_{i>j} X^{-1}(j,i) + N_e \sum_{i>j} X(j,i)]$$

where N(Z,j) is the population density of ion species Z in level j, S(Z-1,j"; Z,j) is the collisional ionization rate (cm^3/sec) from N(Z-1,j") to N(Z,j), α is the sum of the radiative and dielectronic recombination rates ($\alpha_r + \alpha_{dr}$) in cm^3/sec, β is the collisional recombination rate (cm^6/sec), A(i,j) is the spontaneous decay rate from levels i to j (1/sec), X(i,j) is the collisional excitation rate from i to j (cm^3/sec) and X^{-1} is the inverse reaction, collisional de-excitation.

(Note that since this is an equilibrium model, the left hand side of the above equation is set equal to zero.)

Schematically, the transitions and atomic processes considered in this model are:

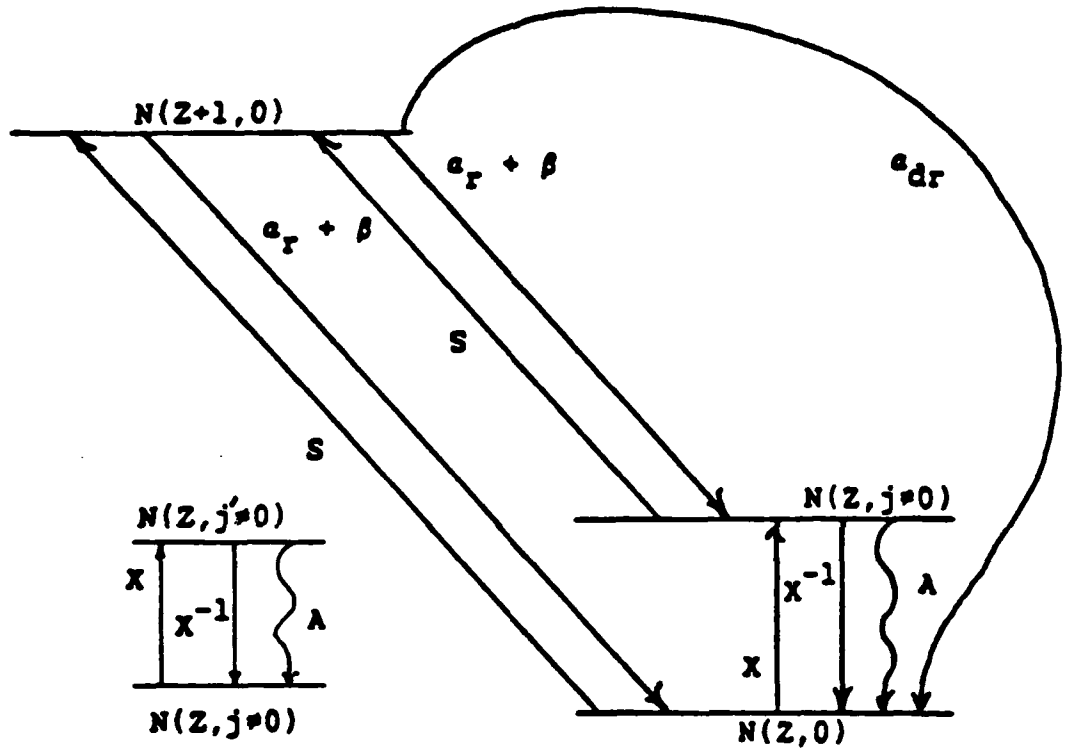

In this form the model consists of an infinite set of coupled non-linear equations, one for each available state of the ions and atoms present in the plasma. Fortunately, there are some methods and procedures available for truncating the number of states. Though we are not explicitly considering reduction in ionization potentials in this model, this phenomenon still sets an upper bound on the number of

discrete quantum states available, i.e., we only need model those states for which $E(n) < E(Z) - \Delta E(Z)$.

In our model we have considered only the 5-10 lowest states for each ionization stage of carbon, including neutral carbon. Although a limited number of states have been considered in this model, they should still be adequate for modelling the radiation field, specific heats and other equations of state information needed for the beam - target simulations.

We have shown that the CRE model is applicable over the range of plasma conditions considered in this work, i.e., for temperatures between 1 and 100 ev and ion densities between 10^{19} and 10^{24} cm^{-3}. Both the CRE and LTE models give identical results for collisionally dominant plasmas. Similarly, the CRE model exhibits coronal behavior in the low density limit. This ability to model both collisional and radiative plasmas is essential for a comprehensive ionization dynamics model.

In addition, we investigated the time constraints placed upon the overall simulation. In particular this consists of a consideration of the equilibrium aspects of the CRE model and the single temperature and fluid assumptions inherent in the hydrodynamics code. In all cases, we found that the models are valid for the timing limitations encountered in this study.

We have calculated temperature, density and pressure profiles for evolving targets. We find that the deposition region heats very rapidly until the processes of electron thermal conduction, radiative loss and beam deposition begin to equilibrate. Once this occurs, we find that the pressure across the width of the deposition region remains fairly constant during the interaction. The pressure is responsible for

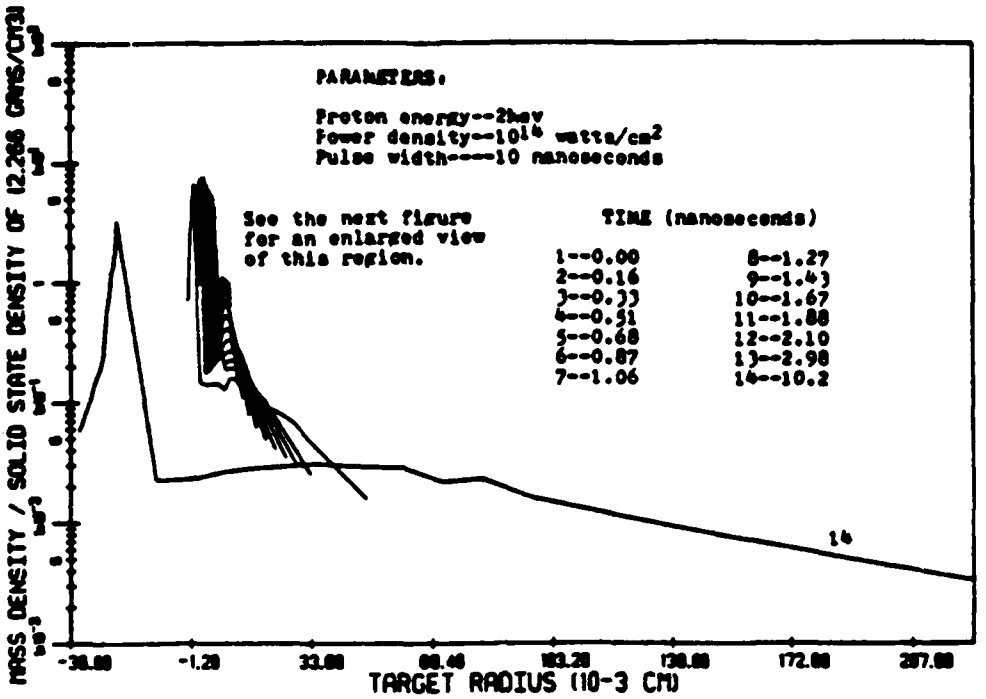

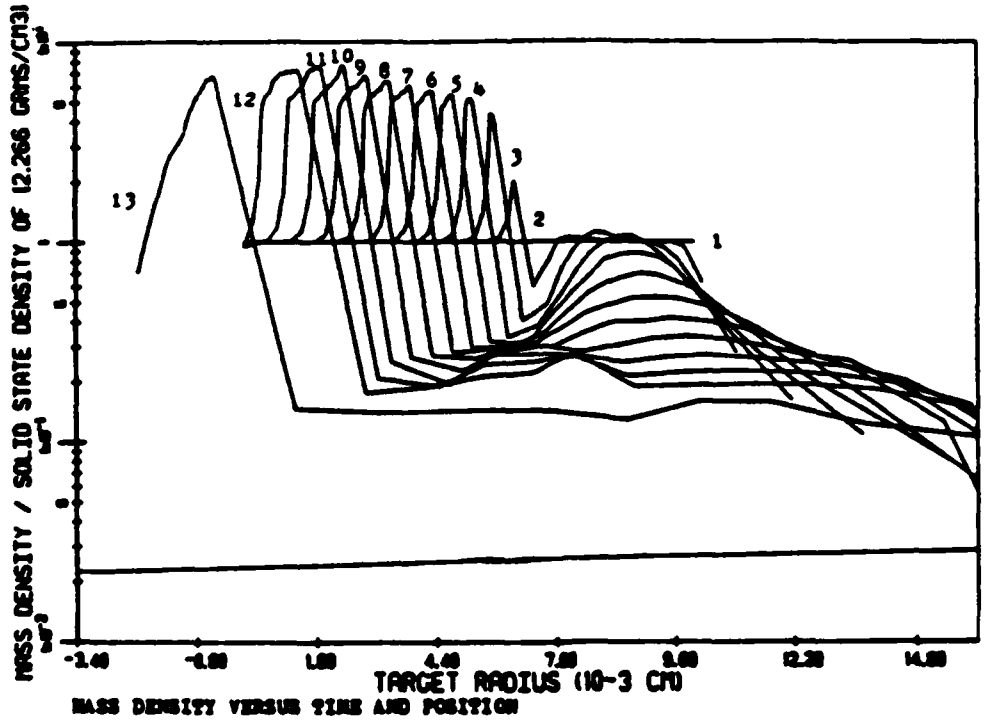

MASS DENSITY VERSUS TIME AND POSITION

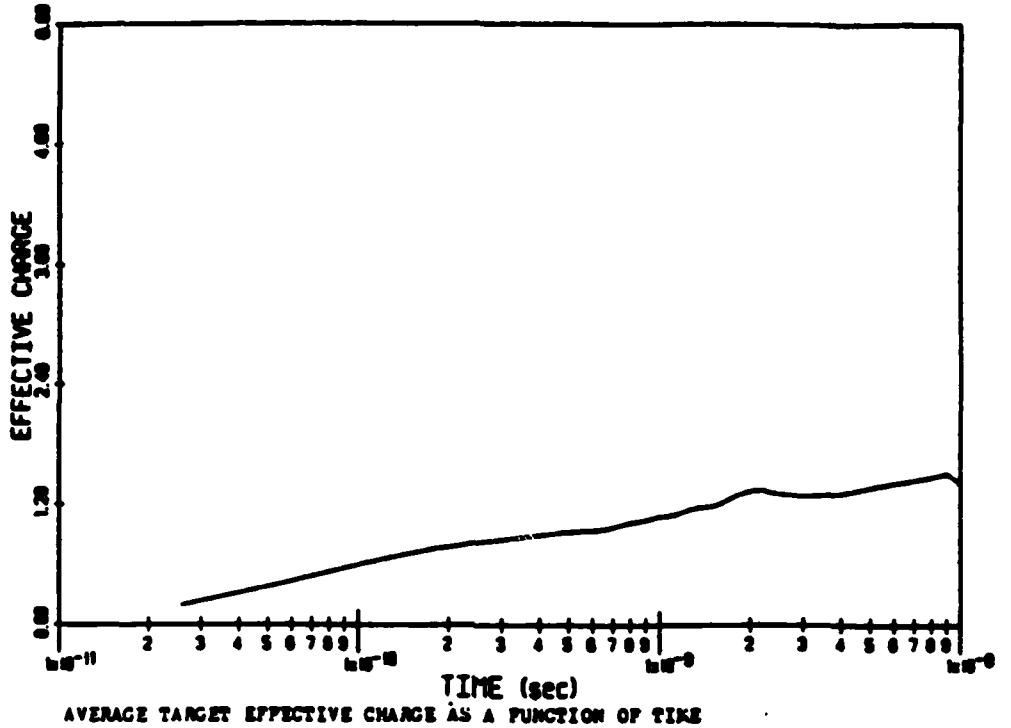

AVERAGE TARGET EFFECTIVE CHARGE AS A FUNCTION OF TIME

FIGURE 4.46

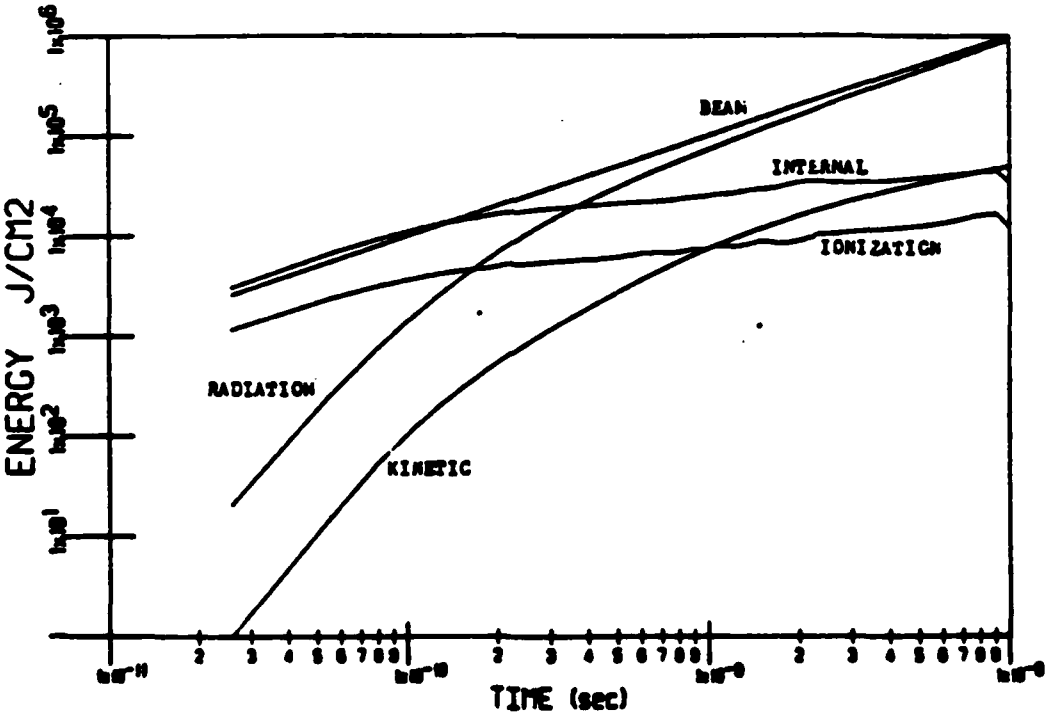

ENERGY PARTITIONING AS A FUNCTION OF TIME

compression of the nondeposition region to densities as high as five to ten times solid state. We provide diagnostic information that displays various transition energies and power densities during the ablation. In addition, the partitioning of the deposited energy into internal, kinetic and radiative components is examined. This model can be applied to a variety of plasma and beam conditions. The plasma restrictions have already been mentioned, and the beam conditions must be such that the energy and power density is sufficient to heat the target to at least several ev (1 ev represents the lower bound of the rate coefficient table).

An examination of the results of our parameter study suggests the direction one might take in order to tailor the energy partitioning of the radiation field or ablation region for a specific application. For example, if carbon is to be used as a x-ray laser pump, then one might want to optimize the radiation conversion efficiency or the shape of the emission profile. In our work, we find that conversion efficiencies can be as large as 90%. We also find that the thermal emission profile is dependent upon both the energy and power density of the beam. This is illustrated by the observation that the hardness of the radiation field can be increased by either using less energetic protons and maintaining the same power density or else increasing the power density. The parameter study also categorizes the dependence of internal, kinetic and radiative energy upon beam power density and proton energy. The radiation field is further divided into relative contributions of line, recombination and bremsstrahlung radiation.

We also investigated the effects of including the inner-shell photon absorption process. This is the only radiation transport we considered

PARAMETER STUDY
(Power density is 10^{12} w/cm^2)

PLASMA "ENERGY" PARAMETERS	INITIAL ION ENERGY 1 Mev	INITIAL ION ENERGY 2 Mev	INITIAL ION ENERGY 3 Mev
ENERGIES IN UNITS OF (10^3 J/CM^2) AND (% OF TOTAL BEAM ENERGY) ARE LISTED			
BEAM	9.0 (100%)	9.0 (100%)	9.0 (100%)
INTERNAL(*)	1.9 (21%)	2.7 (30%)	3.2 (36%)
KINETIC	1.2 (13%)	1.1 (12%)	.95 (11%)
RADIATIVE	5.9 (65%)	5.2 (58%)	4.9 (54%)
***	***	***	***
IONIZATION	.87 (10%)	1.0 (11%)	1.3 (14%)
LINE	3.0 (32%)	2.4 (27%)	2.4 (27%)
RECOMBINATION	1.8 (20%)	1.4 (15%)	1.2 (14%)
BREMSSTRAHLUNG	1.2 (13%)	1.4 (15%)	1.3 (14%)
LINE SPECTRUM ENERGIES (% OF RADIATIVE ENERGY)			
E<10ev	3%	7%	13%
10<E<20ev	15%	26%	28%
20<E<60ev	31%	13%	8%
60<E<100ev	***	***	***
100<E<200ev	***	***	***
200<E<350ev	***	***	***
E>350ev	***	***	***
RECOMBINATION SPECTRUM ENERGIES (% OF RADIATIVE ENERGY)			
E<10ev	***	1%	5%
10<E<20ev	17%	15%	13%
20<E<60ev	13%	9%	6%
60<E<100ev	***	***	***
100<E<200ev	***	***	***
200<E<350ev	***	***	***
E>350ev	***	***	***

* Ionization energy is included in internal energy

PARAMETER STUDY

Power density is 10^{14} w/cm^2)

PLASMA "ENERGY" PARAMETERS	INITIAL ION ENERGY 1 Mev	INITIAL ION ENERGY 2 Mev	INITIAL ION ENERGY 3 Mev
ENERGIES IN UNITS OF (10^5 J/CM^2) AND (% OF TOTAL BEAM ENERGY) ARE LISTED			
BEAM	9.0 (100%)	9.0 (100%)	9.0 (100%)
INTERNAL(*)	.89 (10%)	.45 (5%)	.52 (6%)
KINETIC	.49 (5%)	.47 (5%)	.45 (5%)
RADIATIVE	7.7 (85%)	8.2 (91%)	8.1 (90%)
***	***	***	***
IONIZATION	.22 (2%)	.17 (2%)	.18 (2%)
LINE	2.3 (25%)	2.6 (29%)	1.5 (17%)
RECOMBINATION	4.8 (53%)	4.1 (45%)	3.9 (43%)
BREMSSTRAHLUNG	.60 (7%)	1.5 (17%)	2.6 (29%)
LINE SPECTRUM ENERGIES (% OF RADIATIVE ENERGY)			
E<10ev	***	***	***
10<E<20ev	***	***	***
20<E<60ev	2%	6%	11%
60<E<100ev	***	***	***
100<E<200ev	***	***	***
200<E<350ev	8%	14%	4%
E>350ev	14%	11%	3%
RECOMBINATION SPECTRUM ENERGIES (% OF RADIATIVE ENERGY)			
E<10ev	***	***	***
10<E<20ev	***	***	***
20<E<60ev	***	4%	20%
60<E<100ev	8%	20%	19%
100<E<200ev	19%	18%	8%
200<E<350ev	5%	***	***
E>350ev	30%	7%	1%

* Ionization energy is included in internal energy

in our otherwise "optically thin" model. The results of the study show that as much as 10% of the radiation field can be absorbed by the inner-shell process. Although, for an optically thick application this value would be reduced because of competition with valence photo-processes, it still represents an important absorption mechanism for recombination radiation. An examination of the temperature, density and pressure profiles show that inner-shell photon absorption primarily affects the temperature and density profiles of the ablation region. The nondeposition region appears to be insulated from its effects; thermal conduction and ion shock heating remain the principal heating mechanisms in this region.

Another application investigated was the calculation of the amount of K_α photon energy emitted by the direct interaction of the beam protons with the target atoms. We found that under optically thin conditions, the energy density of the emission is several orders of magnitude below that of the primary radiation field. However, since the energy of the K_α is larger than the other photons, it should be easily resolvable. It was noted that this situation only arises when the target is relatively cold. Otherwise, there will be a significant component of high energy photons created by valence transitions that will also be absorbed by the K shell. When this happens, additional K_α emission is produced and it washes out the beam K_α results. Because the spectrum of K_α depends upon the binding energy of the K shell electron of the emitting atom, it represents a measure of the ionization state of the target.

In conclusion, we feel that this model contains enough essential physics to be useful for analyzing a variety of processes that occur

during the ablation of a carbon target. The processes which we examined in this investigation included: 1) the effects of initial beam conditions on plasma parameters such as kinetic, internal and radiative energy, 2) inner-shell photon absorption and 3) K_α emission due to the direct interaction of the beam particles with target atoms. With the implementation of the suggestions for improvement listed above, the model should be adequate for providing accurate diagnostic information for a variety of physical problems.

References for Section I

1. E. Bonderup, K. Dan. Vidensk. Selsk. Mat.-Fys. Medd. 35, No. 17 (1967).
2. T. L. Ferrell and R. H. Ritchie, Phys. Rev. B16, 115 (1977).
3. Y.-K. Kim and K. Cheng, Phys. Rev. A22, 61 (1980).
4. U. Fano and J. E. Turner in Publication 1133 (National Academy of Sciences, National Research Council, Washington, DC, 1964) p. 49.
5. J. Lindhard and M. Scharff, K. Dan Vidensk. Selsk. Mat.-Fys. Medd. 27, No. 15 (1953).
6. H. H. Andersen et. al., Phys. Rev. A16, 1929 (1977).
7. C. Deutsch, Laser and Particle Beams 2, 449 (1984).
8. F. Bloch, Ann. Physik 16, 285 (1933).
9. J. M. Anthony and W. A. Lanford, Phys. Rev. A25, 1868 (1982).
10. H. H. Andersen, Physica Scripta 28, 268 (1983).
11. P. Sigmund and D.-J. Fu, Phys. Rev. A25, 1450 (1982).
12. G. Maynard and C. Deutsch, Phys. Rev. A26, 665 (1982).
13. F. Herman and S. Skillman, "Atomic Structure Calculations," (Prentice-Hall, N.J., 1963).
14. J. M. Peek, Phys. Rev. A26, 1030 (1982).
15. E. J. McGuire et. al., Phys. Rev. A26, 1318 (1982).

II. Experimental Progress

IIa) Neutral/Ion Interactions with a Laser Ablation Plasma

The attenuation of beam current density is governed by the product of plasma density and interaction cross section integrated over the beam particle path length in the plasma, illustrated in Figure 1. While Coulomb collisions account for the attenuation of an ion beam, neutral particles may undergo charge exchange, momentum scattering, and impact ionization with plasma ions, along with ionization by impact with plasma electrons. The Coulomb cross section is calculated from an expression obtained by integration of the Rutherford scattering formula. Of the neutral interaction cross sections, the charge exchange cross section appears to be the largest and is to date the only one for which we have found adequate experimental and theoretical treatment in the literature[1] ($H^o + C^{+q}$ interactions). For a 10 keV hydrogen atom in a C^{+q} plasma, we estimate for the total neutral interaction cross section

$$\sigma \sim \sigma_{cx} \sim 5 \times 10^{-15} \text{ cm}^2$$

Beam attenuation predictions are presented in Figure 2 for the case of 10 keV protrons or hydrogen atoms traveling 20cm through a quiescent, 20eV carbon plasma of various densities. Fokker-Planck calculations of initial beam particle slowing down (τ_s) and diffusion (τ_b) times indicate that path lengths much greater than 20 cm would be required for the beam particles to acquire an isotropic velocity distribution and to thermalize with the plasma, since a 10 keV proton will travel 20 cm in about 140 ns. However, since the Coulomb cross section is so large for the conditions considered, all beam

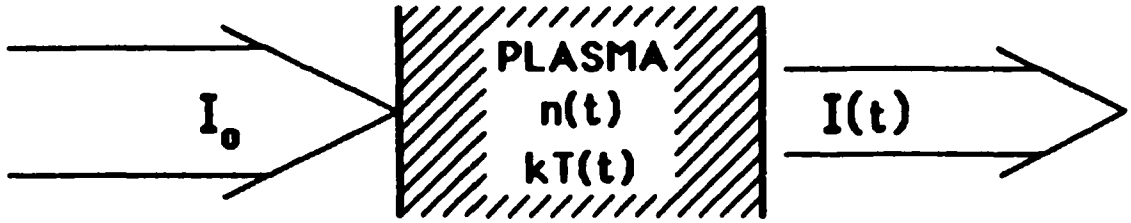

Ion beam attenuation:

$$I(t) = I_o \exp\left\{-\int n_p \sigma_c \, dl\right\}$$

where σ_c = Coulomb scattering cross section

Neutral beam attenuation:

$$I(t) = I_o \exp\left\{-\sum_{i,z} \sigma_{i,z} \int_{l_p} n_{i,z} \, dl - \frac{\langle \sigma_e v_e \rangle}{v_b} \int_{l_p} n_e \, dl\right\}$$

where $\sigma_{i,z}$ = cross section for charge exchange, σ_{cx},
+ momentum scattering, σ_s,
+ impact ionization, σ_{ii},
with plasma ions of species i,
charge z, and density $n_{i,z}$;

$\langle \sigma_e v_e \rangle$ = electron impact ionization cross section averaged over the electron velocity distribution;

v_b = beam particle velocity;

l_p = beam path length in the plasma.

Figure 1 - Plasma attenuation of a particle beam.

ions will undergo Coulomb collisions while traversing the plasma and hence will be lost from the beam. With 10 keV hydrogen atoms, on the other hand, we predict significant attenuation by charge exchange interactions to occur for plasma line densities greater than about 10^{12} cm^{-3}.

With the assumption of cross sections which are independent of space and time, we see in Figure 1 that the time behavior of the beam current density exiting the plasma depends on the time behavior of the integral of plasma density over beam particle path length in the plasma, which is defined in terms of the line density along the particle beam axis. An expression for the line density resulting from the production of a laser ablation plasma is obtained from the integration of Tallents' expression[2] for the ablation plasma ion density, presented in Figure 3. The laser beam is taken to be perpendicular to both the particle beam axis and the target surface. The buildup and decay of the line density after firing the laser is also presented in Figure 3.

IIb) Duopigatron Based Experiments Concerning Neutral/Ion Beam Interactions with Laser Ablation Plasmas

During the past year our experimental efforts have been concentrated toward the measurement of the effects of an independently-produced ablation plasma upon the penetration of a neutral or ion beam to an underlying surface. This problem has relevance to the case of a plasma or gas cloud surrounding an outgassing material in a space vacuum environment.

- 10 keV proton beam, C^+ plasma*

$\sigma \sim \sigma_c$ (Coulomb scattering), KT ~ 20 eV

n $[cm^{-3}]$	σ_c $[cm^2]$	τ_s [s]	τ_D [s]	l_{mfp} [cm]	$\frac{I}{I_0}$
10^{11}	5×10^{-4}	2×10^{-2}	2.55	2×10^{-8}	~ 0
10^{12}	4×10^{-5}	2×10^{-3}	0.28	2×10^{-8}	~ 0
10^{13}	5×10^{-6}	2×10^{-4}	0.03	2×10^{-8}	~ 0
10^{14}	4×10^{-7}	2×10^{-5}	0.003	2×10^{-8}	~ 0

- 10 keV neutral hydrogen beam, C^+ plasma*

$\sigma \sim \sigma_{cx} \sim 5 \times 10^{-15}\ cm^2$ (ref. 1)

n $[cm^{-3}]$	l_{mfp} [cm]	$\frac{I}{I_0}$
10^{11}	2000	0.99
10^{12}	200	0.90
10^{13}	20	0.37
10^{14}	2	~ 0

*Assumed uniform and stationary ($\bar{n} = n L$, L = 20 cm)

Figure 2- Beam attenuation predictions.

Ion number density :

(G. J. Tallents, Laser and Particle Beams (1983), Vol. 1, Part 1, pp. 171-80.)

$$n(R,\theta,t) = \frac{2\pi^{-3/2} N_T \; k^2}{(v_z^\bullet)^3 \; t^3} \exp\left\{ \frac{-R^2\left[(k^2-1)\sin^2\theta + 1\right]}{(v_z^\bullet)^3 \; t^3} \right\}$$

Line density along particle beam axis, located a distance $z_\bullet$ from target surface:

$$\bar{n}(z_\bullet,t) = \int n(z_\bullet,\theta,t)\, dl$$

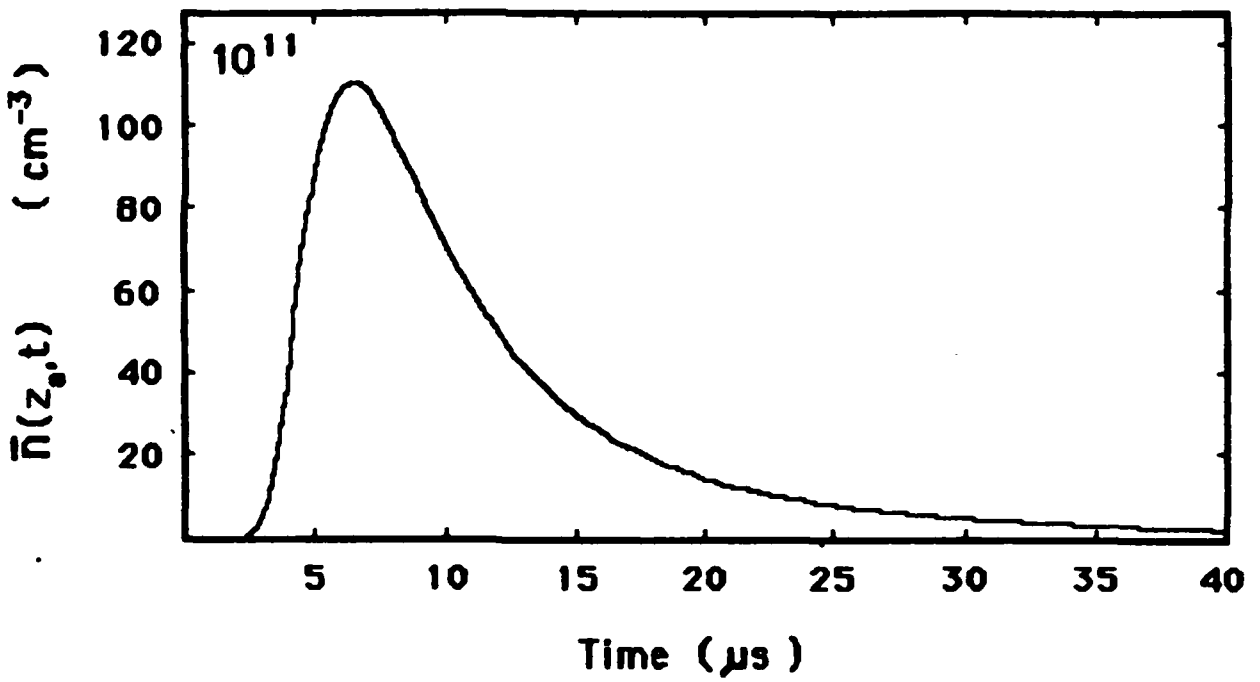

Conditions: $z_\bullet = 1$ cm, L = 20 cm, $v_z^\bullet = 5 \times 10^6$ cm/s,

$$k = \frac{v_z^\bullet}{v_r^\bullet} = 4, \quad N_t = 10^{15} \text{ ions.}$$

Figure 3 - Self-similar expansion model for laser-produced target plasma.

IIb.1) Beamline and Vacuum Systems

The duopigatron based experiment has been completely disassembled and renovated for these experiments. What was needed for these interaction experiments was a highly collimated ion or neutral beam to interact with the expanding carbon ablation plasma produced by a ruby laser. A floor plan showing the present location of the components in this experiment is shown in Figure 4. Major components and changes in the system will be discussed in the following sections.

The neutral beam device is depicted as it existed immediately following its renovation in Figures 5 and 6. Large port gate valves are used to isolate components of the system. The beamline expands from the 10.2 cm diameter opening between the neutralization tank and the vertical gate valve to the 15.2 cm diameter opening into the target chamber, which is a 29 cm diameter, 33 cm long stainless steel tank. Following vacuum leak and electrical system checks, 10 kV hydrogen beams were extracted and monitored to verify proper operation.

In order to place diagnostics so as to monitor the beam after passage through a target plasma, a number of changes were made to the system. First, in order to avoid filling the target chamber with a background plasma produced by passage of the beam into the chamber, and to better collimate the particle beam entering the chamber, a 3 cm aperture was placed at the chamber entrance. Better results were obtained by adding two more apertures, one just after the vertical gate valve and another just after the second pumping station. This arrangement provided both a collimated particle beam and differential pumping.

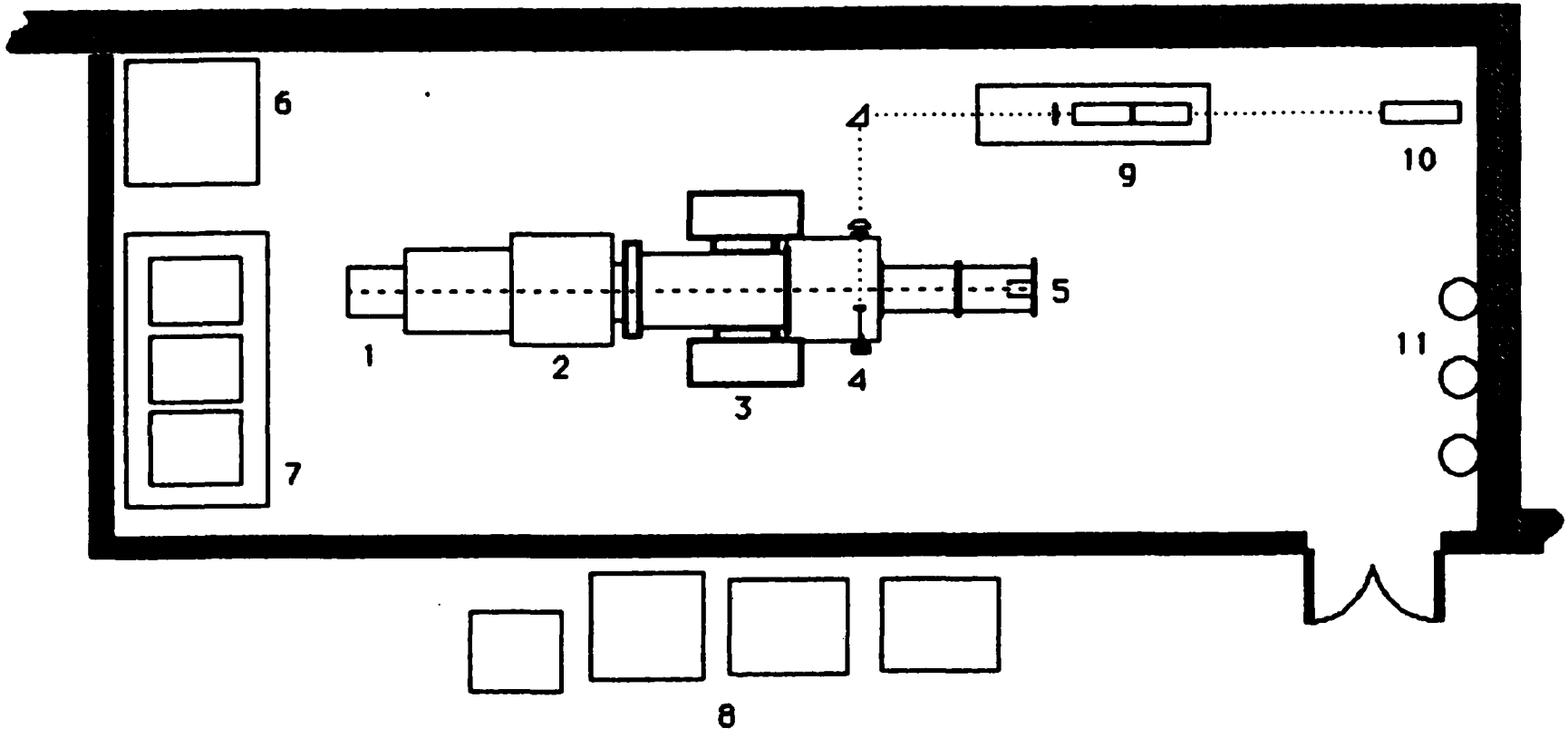

Figure 4 - Components of the beam interaction experiment. Shown is (1) the duopigatron, (2) neutralization cell, (3) bending magnets (4) target chamber, (5) particle detector, (6) isolation transformer, (7) isolated power supplies, (8) controls, (9) ruby laser, (10) HeNe laser, (11) gas bottles. Not shown is the high voltage power supply located in a separate interlocked room.

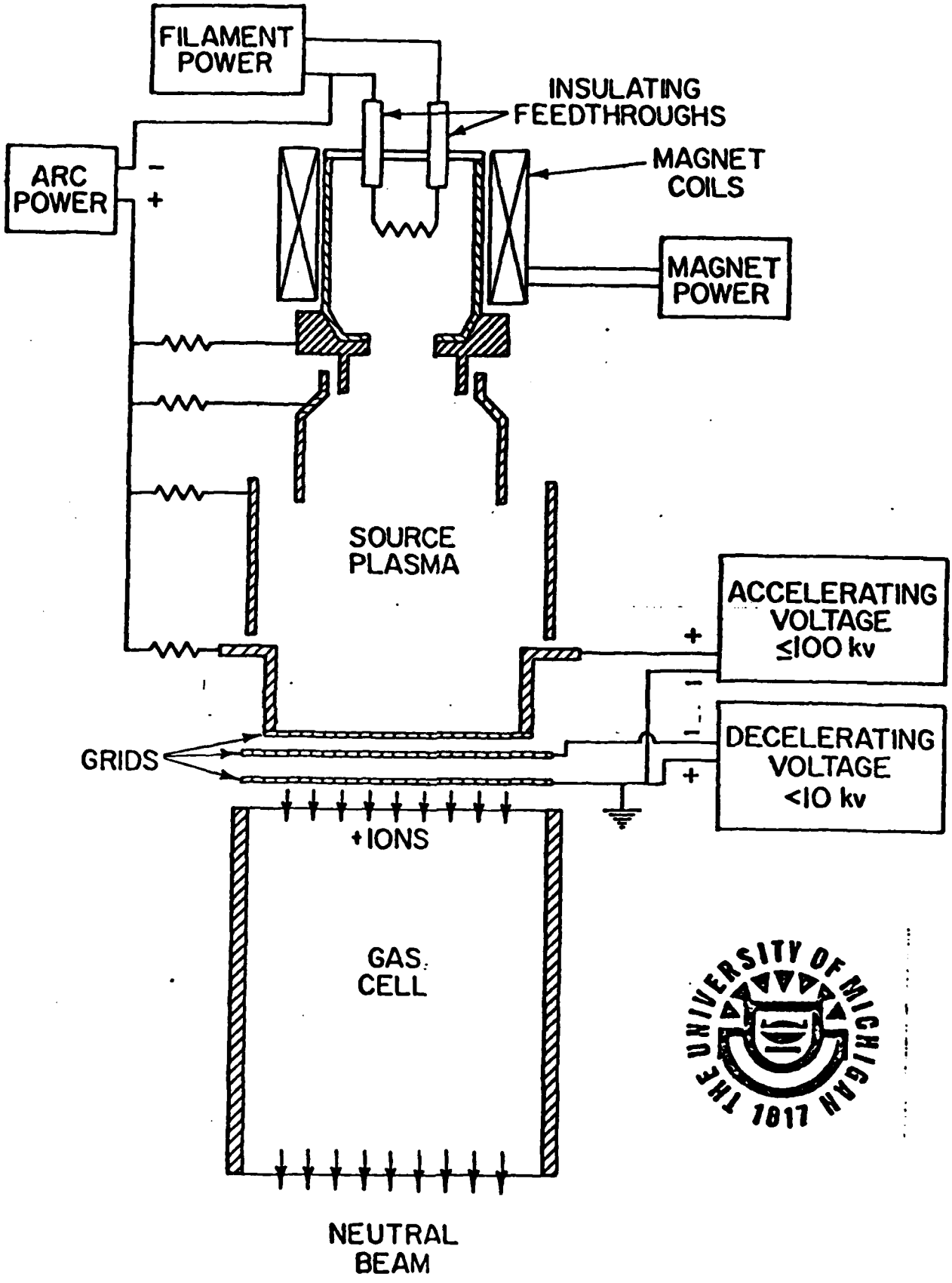

Figure 5 - Schematic illustration of duoPIGatron type positive ion source with accelerating grids and neutralizing gas cell.

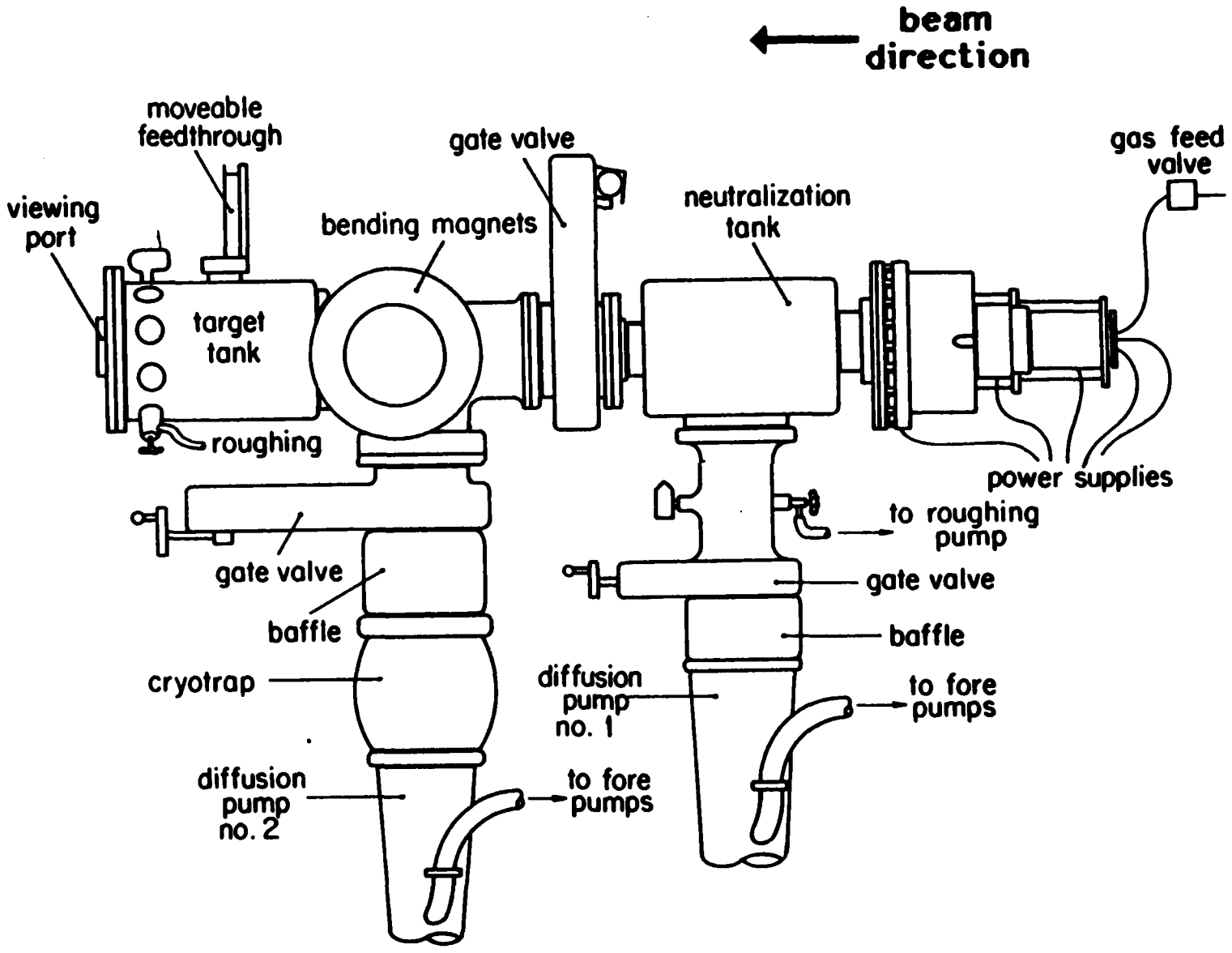

Figure 6 - Duoplgatron and beamline as constructed at the beginning of this reporting period.

Pressure in the target chamber remains below 10^{-5}Torr while the pressure in the duopigatron end rises to nearly 10^{-3}Torr when a beam is extracted. Second, since the experimental targets are to be located in the plane defined by the 11 ports arranged circumferentially near the end of the chamber, a 10 cm I. D. Pyrex cross was attached to the target chamber end flange to allow the mounting of diagnostics downstream of the target. Initial experiments using this arrangement indicated the need to move the diagnostics further away from the target, due to target plasma streaming and particle beam timing, and so a second Pyrex section was placed between the first one and the chamber end flange. Further studies indicated the need for additional apertures to be placed between the target plasma and the Pyrex system along with a reduction of the size of the aperture at the entrance to the target chamber. The aperture into the Pyrex system made it necessary to install a third vacuum pumping station. The target end of the neutral beam device, as of the end of this reporting period, is illustrated in Figure 7.

IIb.2) Ruby Laser System

A target plasma is produced in the target chamber by focusing the output of a Korad K-15 ruby laser onto a solid target mounted within the chamber on the end of a rotatable feedthrough. A 29 cm focal length lens is mounted external to the vacuum system and the laser beam passes through a glass window. A prism is used to turn the laser beam and a HeNe laser is used to align the laser system components, which are

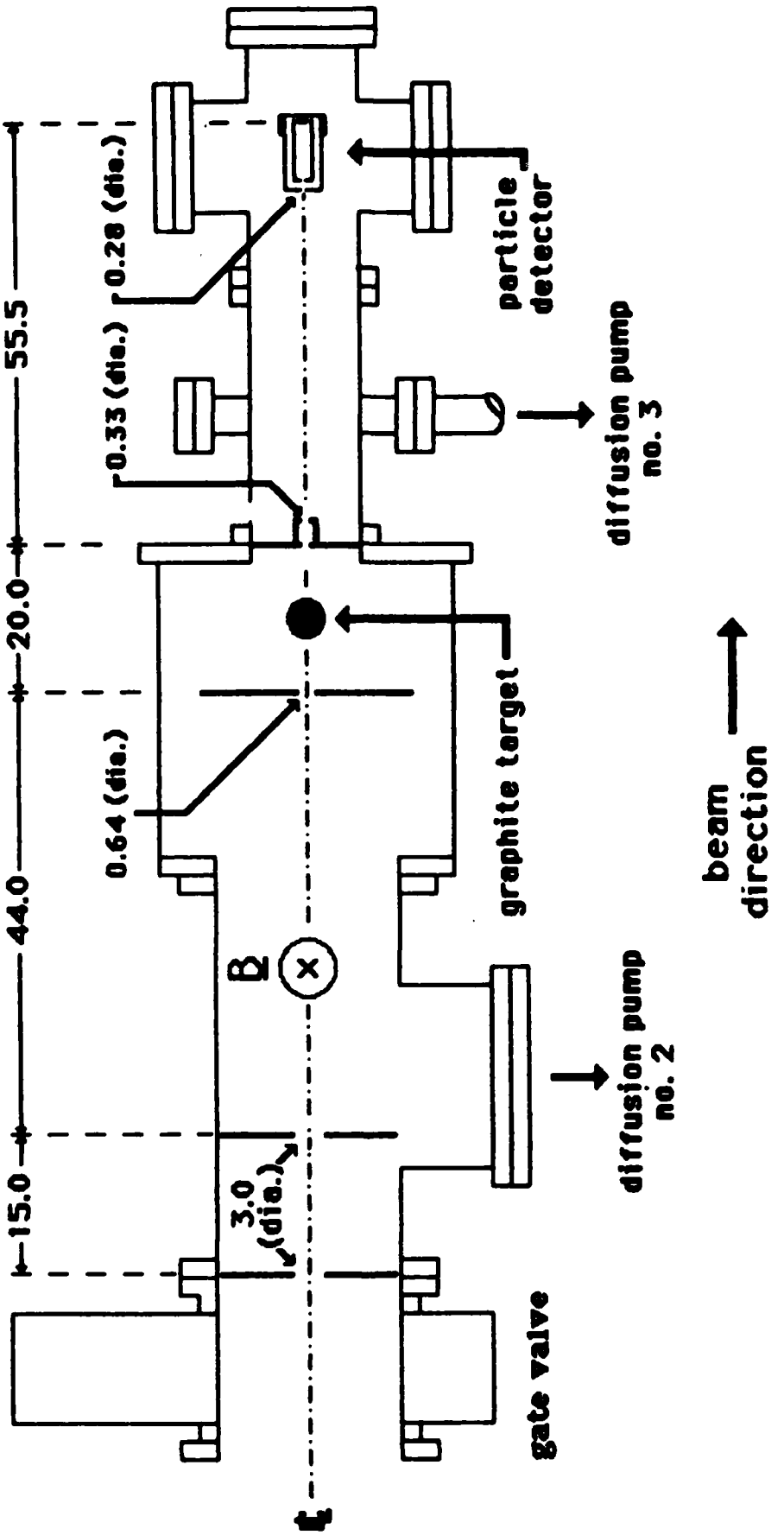

Figure 7 - Target end of beamline. (dimensions in cm)

shown in Figure 4. A pockels cell allows conversion of the laser output from the relaxation mode to the Q-switched mode.

IIb.3) Diagnostics

Beam attenuation data is obtained by the use of a Faraday cup type of particle detector, illustrated in Figure 8. In this device, an energetic particle (ion or neutral) strikes the collection plate, which then emits secondary electrons. The secondary electrons are collected by the innermost cup, which is typically biased at +15 VDC. The outer cups define the collector's acceptance angle and help to shield the innerccup from any charged background particles. Ions collected on the emitting plate and electrons leaving the plate produce a measurable voltage signal across the resistor shown in the figure.

Other beam parameters monitored during each shot are: 1) Arc current, I_{arc}, the current flowing from cathode to anode in the duopigatron; 2) Drain current, I_{drain}, the current drawn by the accelerator grid; and 3) Accelerator voltage, V_{accel}, the voltage applied to the accelerator grid. Arc current is obtained by measuring the voltage across a shunt resistor, drain current is obtained through the use of a Pearson coil on the transmission line between the high voltage capacitor and the accelerator grid, and the voltage on the accelerator grid is measured with a high voltage probe.

IIb.4) Ion and Neutral Beam Probe Measurements

The first task performed after the renovation and subsequent system checkout was to determine the parameters of the particle beam in order to adjust the geometry of the interaction

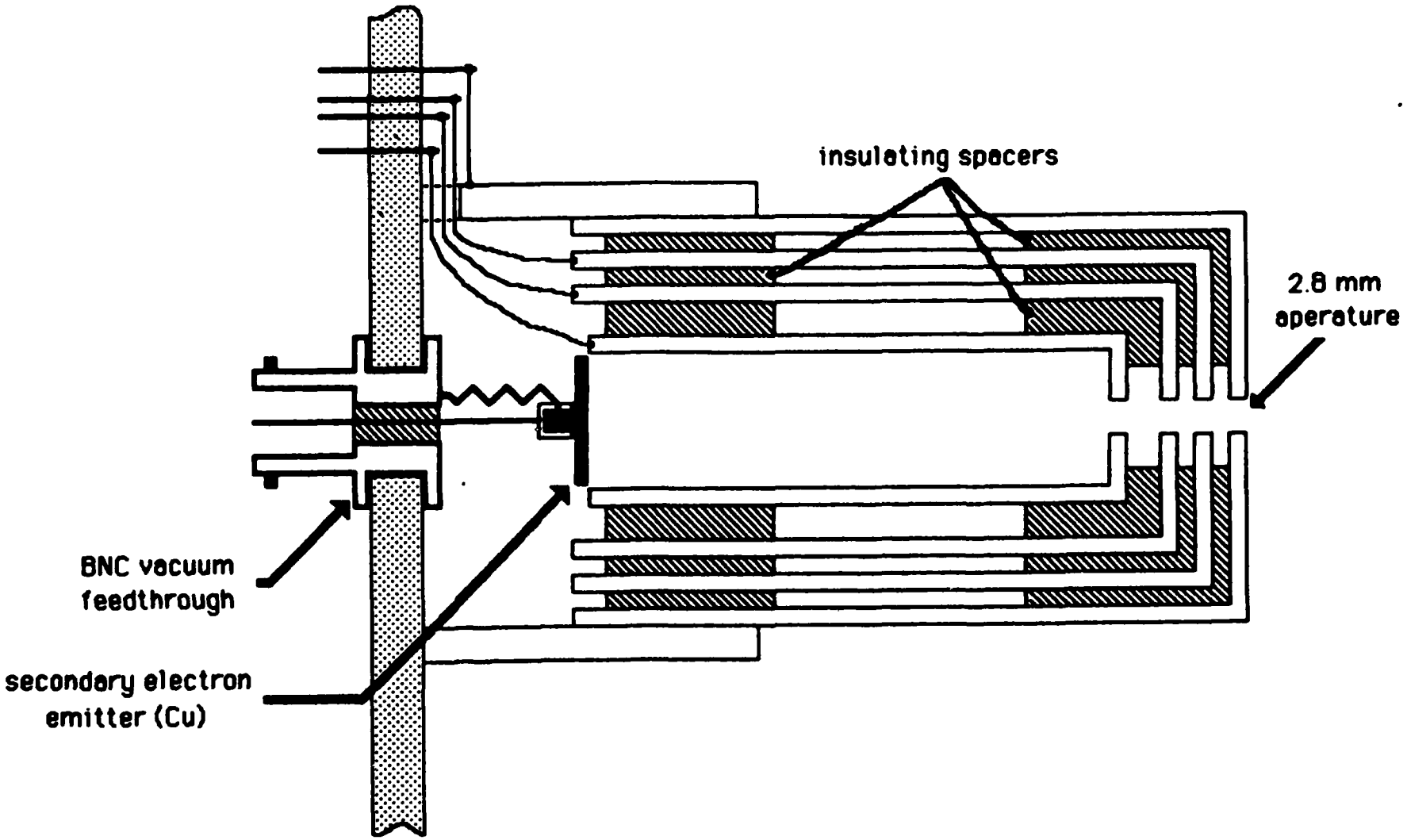

Figure 8 - The particle cetector as mounted on a plexiglass end flange.

experiment. In preparation for the target interaction experiments, a Pyrex tee was attached to the target chamber end flange and the detector was mounted on a movable feedthrough. A ruled marker was used to indicate the cup position relative to the beamline axis and the cup was repositioned between shots to scan across the beam diameter.

Typical oscilloscope traces showing the timing and beam parameters for 20 amp arc discharges and an accelerating voltage of 10 kV are presented in Figure 9.

Figure 10 presents the results of a vertical scan of beams after having passed through the single 3 cm aperture for both 0 and 5 amps of bending magnet current (0 and approx. 180 Gauss). The factor of three decrease in the peak signals for such a low bending magnet current indicates that the beam ion fraction is quite high and the degree of beam divergence is indicated by the width of the curves: For these non-optimal conditions, more than 70% of the beam particles entering the target chamber are ions and the beam expands from 3 cm to about 6 cm in diameter in a distance of 37 cm. Fixing the cup position at 2 cm from the beamline axis and varying the current through the bending magnets yielded the results presented in Figure 11. This shows that 20 amps (approx. 700 Gauss on axis) removes all but the heaviest of beam contaminants and, again, that only about 30% of the beam particles are charge neutral.

Figures 10 and 11 were obtained from operation of the source with a relatively high hydrogen gas feed rate (gas

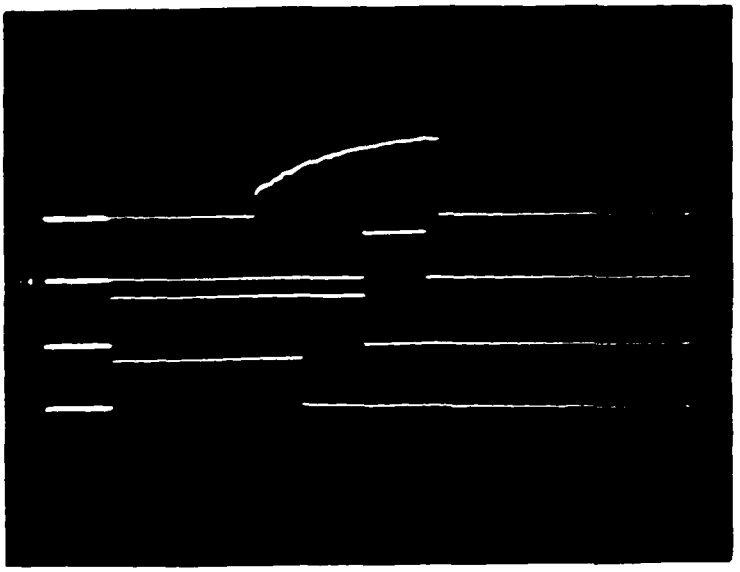

A. 0.1 s/cm

1 - I_{arc}, 5 V(20 A) /cm

2 - flashlamp trigger, 5 v/cm

3 - arc voltage gate, 5 V/cm

4 - gas feed gate, 5 V/cm

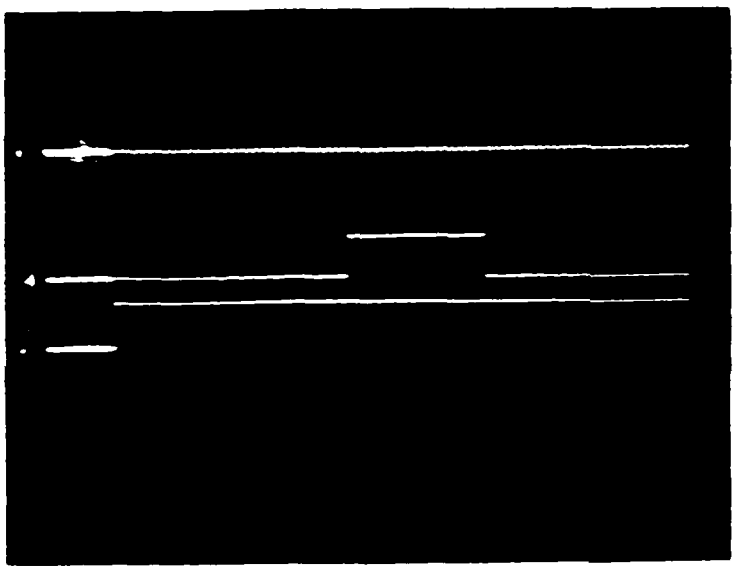

B. 200 µs/cm

1 - I_{arc}, 5 V(20 A)/cm

2 - accelerating voltage trigger, 5 V/cm (crowbarred 400 µs later

3 - flashlamp trigger, 5 V/cm (Q-switched 1 ms later)

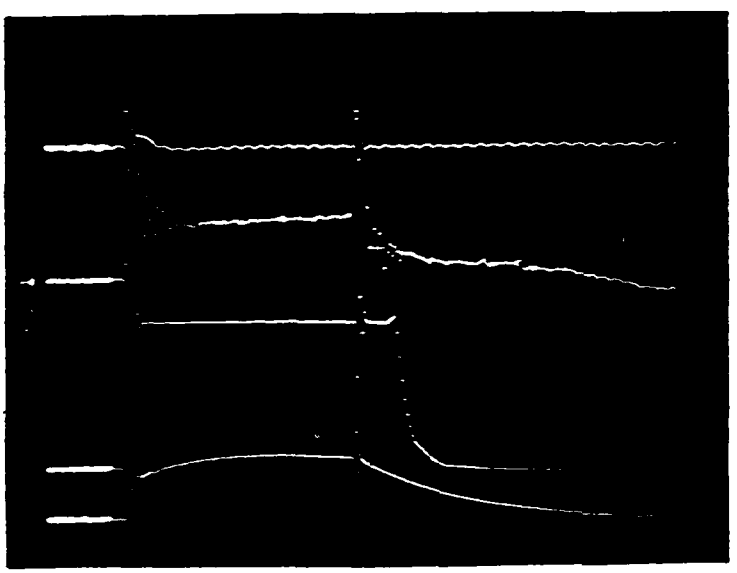

C. 100 µs/cm

1 - I_{arc}, 5 V (20 A)/cm

2 - I_{drain}, 50 mV (0.5 A)/cm

3 - I_{detec}, 2 V (0.8 µA)/cm

4 - V_{accel}, 5 V/cm (x 2000)

Figure 9 - Typical hydrogen beam parameters.

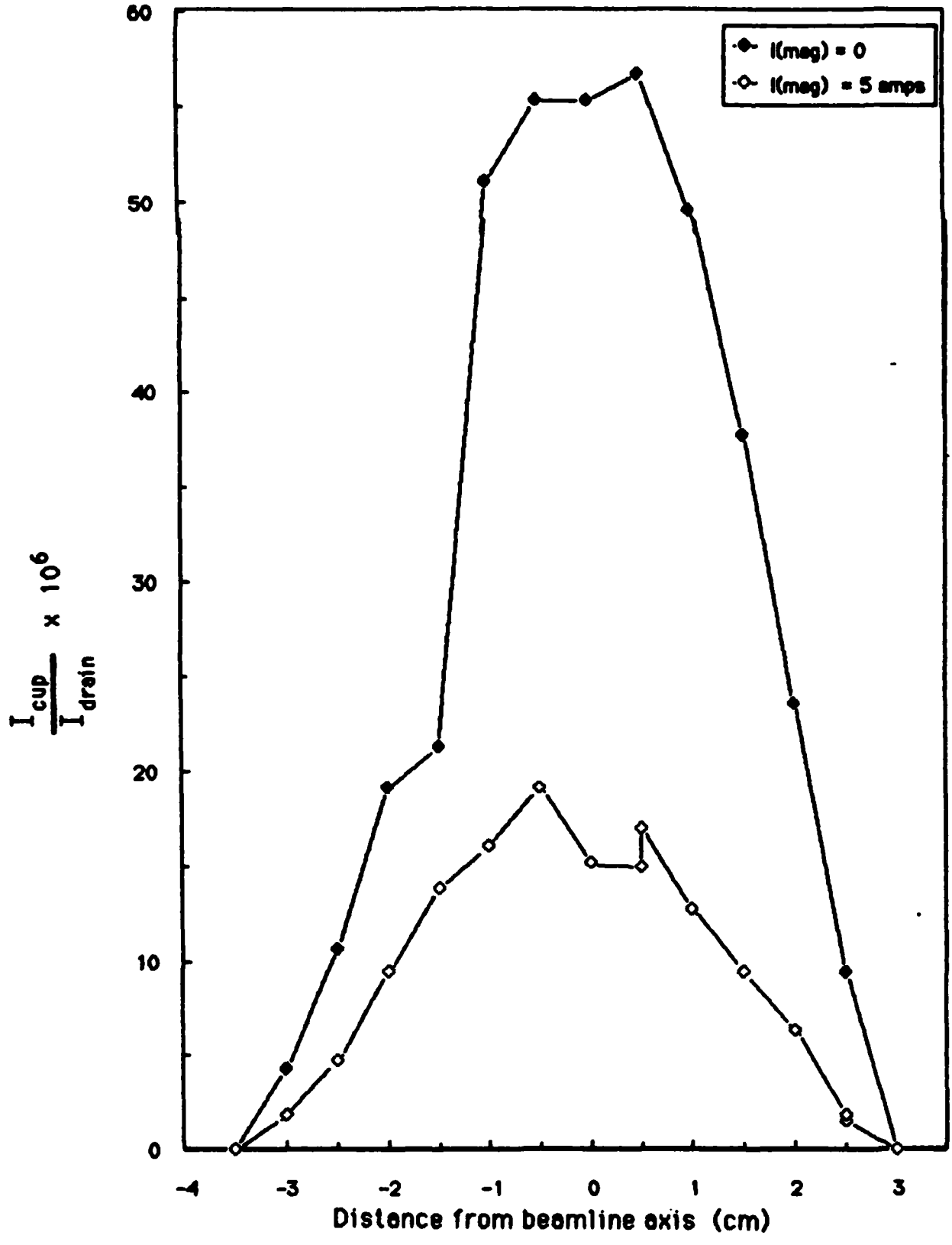

Figure 10 - Beam profile using a single 3 cm aperature.

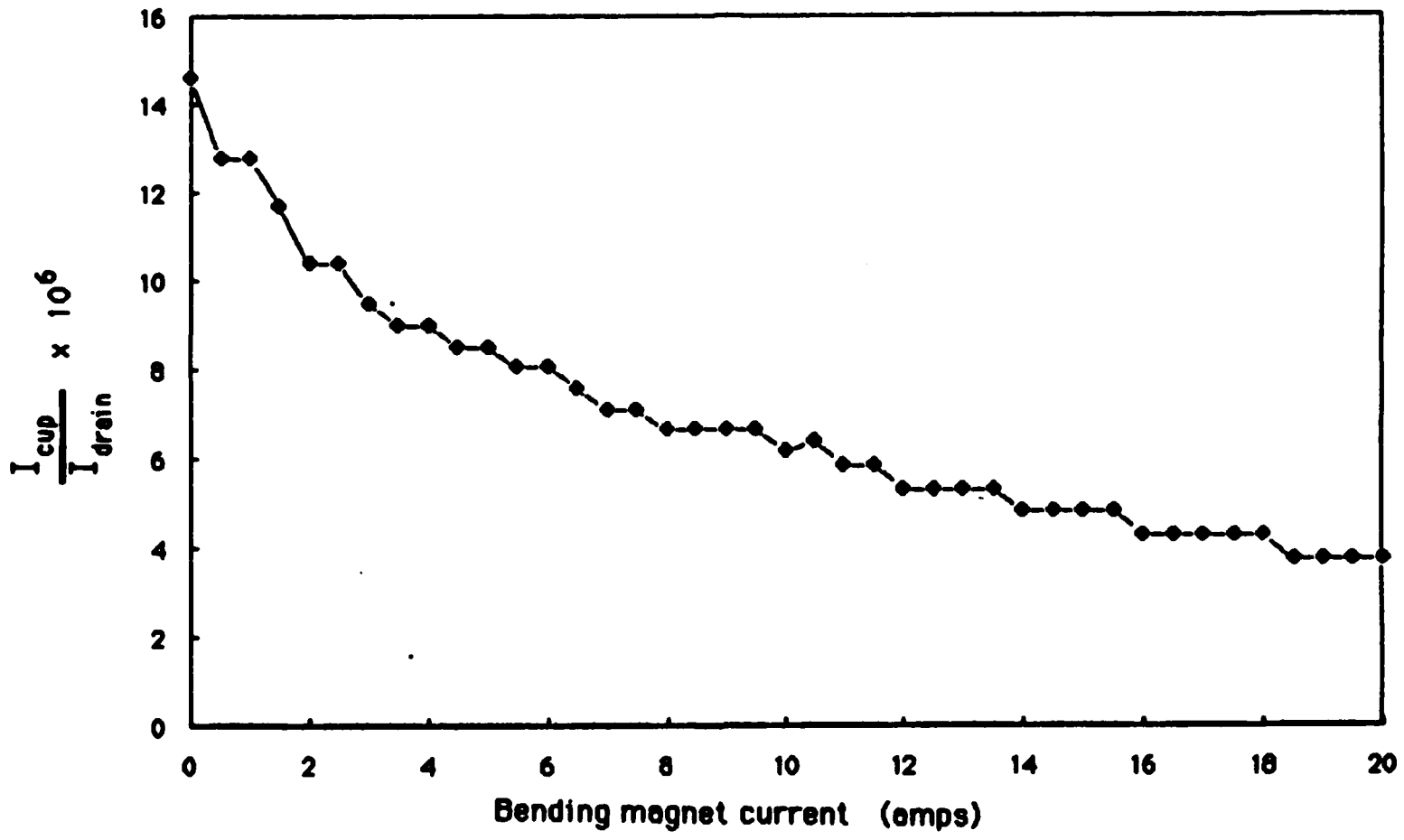

Figure 11 - Normalized detector current vs. bending magnet current.

valve setting = 100). In an effort to increase the beam neutral fraction and to improve beam collimation, two additional 3 cm diameter apertures were placed in the beamline as shown in Figure 7. With the detector placed on the beamline axis, 10 kV hydrogen beams were again extracted from 20 amp arc discharges, this time varying the gas feed rate. Results for bending magnet currents of 0 and 20 amps are presented in Figure 12, which show that the neutral fraction of the beam increases as the gas feed rate decreases, as expected, since there are fewer background particles available for the neutrals to charge exchange with (back into ions) in the beamline. However, there is a lower bound on the gas feed rate and gas pulse length, below which there is no source plasma buildup. This limit appears to be at a gas valve setting of approximately 50 and a gas pulse length of about 0.3 seconds for the aperture placement shown in Figure 7. Discharges at this operating point are very unstable.

Finally, with the gas valve setting at 60 and gas pulse length of 0.3 seconds, the cup was again scanned across the beam diameter to obtain the results shown in Figure 13. Although the apertures have reduced the beam current entering the target chamber, these results clearly show that neutral fraction under these conditions is now on the order of 90% and that the beam collimation is somewhat improved.

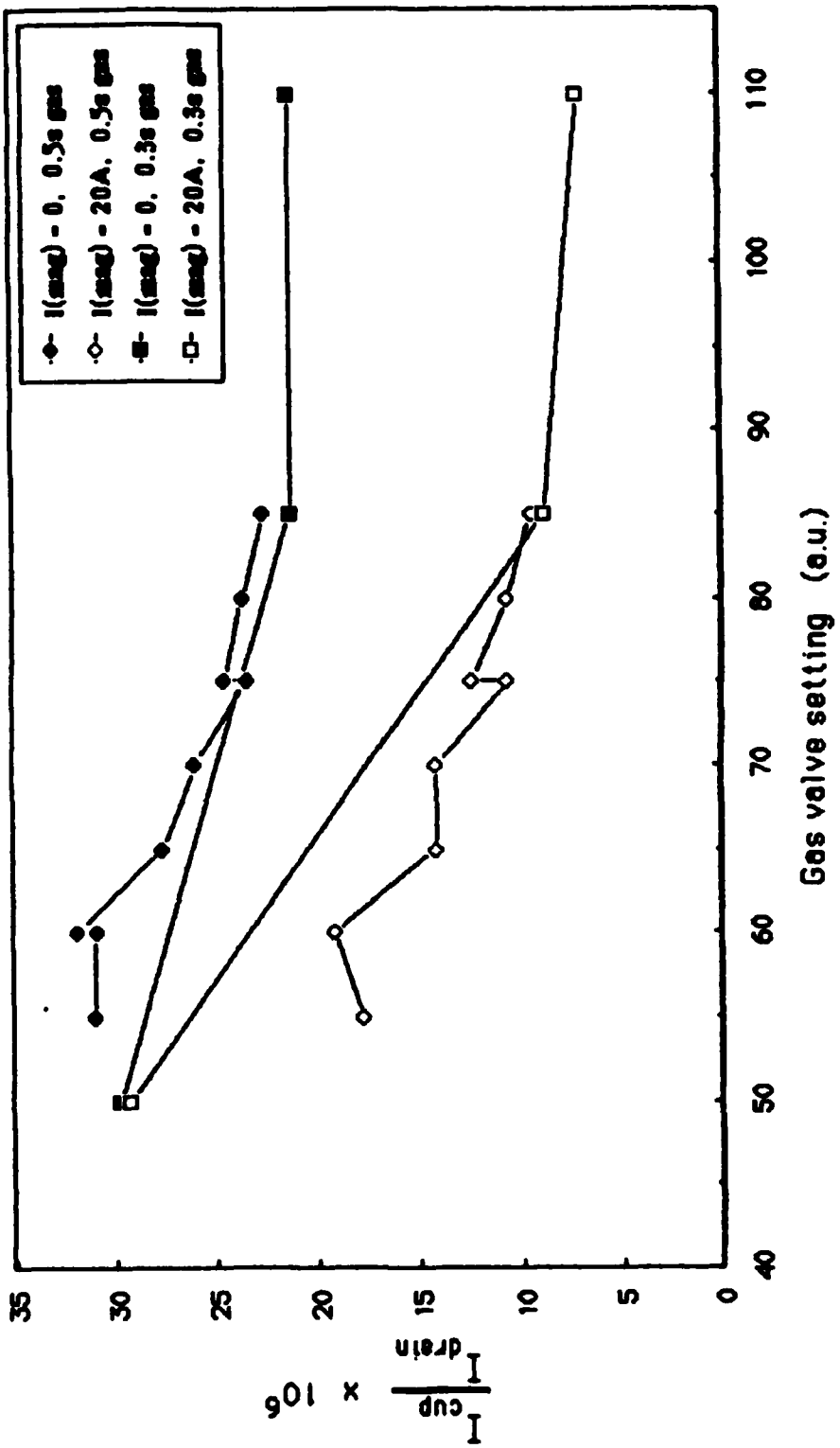

Figure 12 - Normalized detector current vs. gas valve setting.

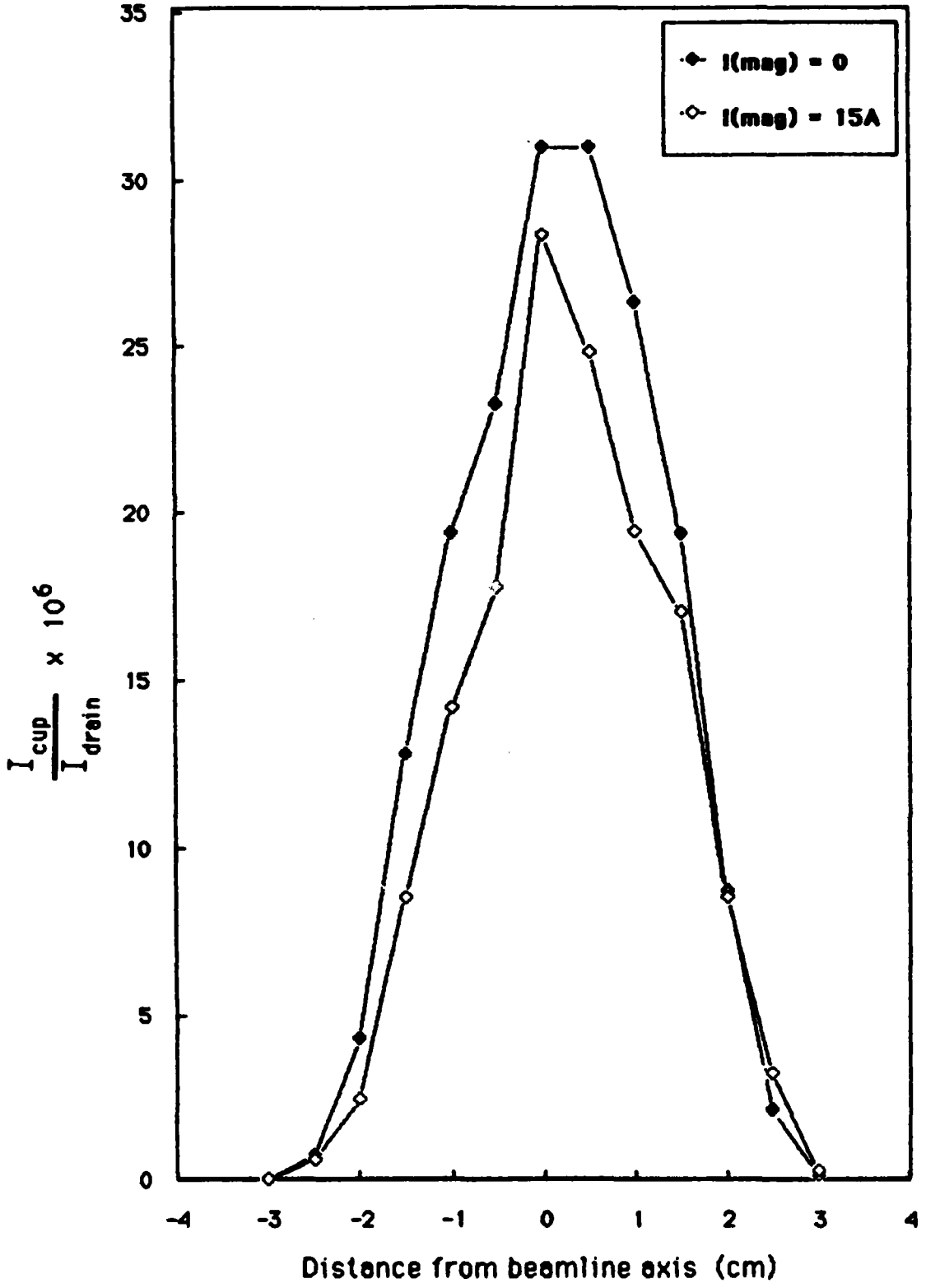

Figure 13 - Beam profile using three 3 cm aperatures.

IIb.5) Ablation Plasma Production and Diagnostics

The production of an ablation plasma involved focussing the ruby laser output onto the surface of a solid target: A plume of ionized target material expands from the surface at a velocity on the order of 10^6 cm/sec. The total number of particles emitted and their energy depends on the energy delivered by the laser. Initial use of the ruby laser involved its operation in the relaxation mode, which can deliver up to about 1.2 Joules. However, in order to facilitate the correlation of laser output with diagnostic signals, the laser has been operated during this period in the Q-switched mode, which delivers up to about 0.3 Joule with a pulse width of 40-60 ns. Oscillograph traces from PIN diode detection of the laser output in both modes are presented in Figure 14.

Prior to this reporting period, carbon plasmas were produced using the relaxation mode output and attempts were made to characterize them. These initial studies involved the use of flat copper plates, biased at various voltage, to collect the charged plasma particles. With the plates located 1.55 and 2.55 cm from the face of the graphite target, it was determined that the electron temperature is in the range $16 < kT(eV) < 24$, that the maximum ion velocity is about 2×10^6 cm/s, which, for carbon ions, yields an average expansion energy of 6.2 eV.

More recently, Q-switched laser produced carbon plasma has been studied through the use of a Langmuir probe in order to obtain an estimate of the plasma electron temperature. With the laser beam axis perpendicular to the graphite target, the

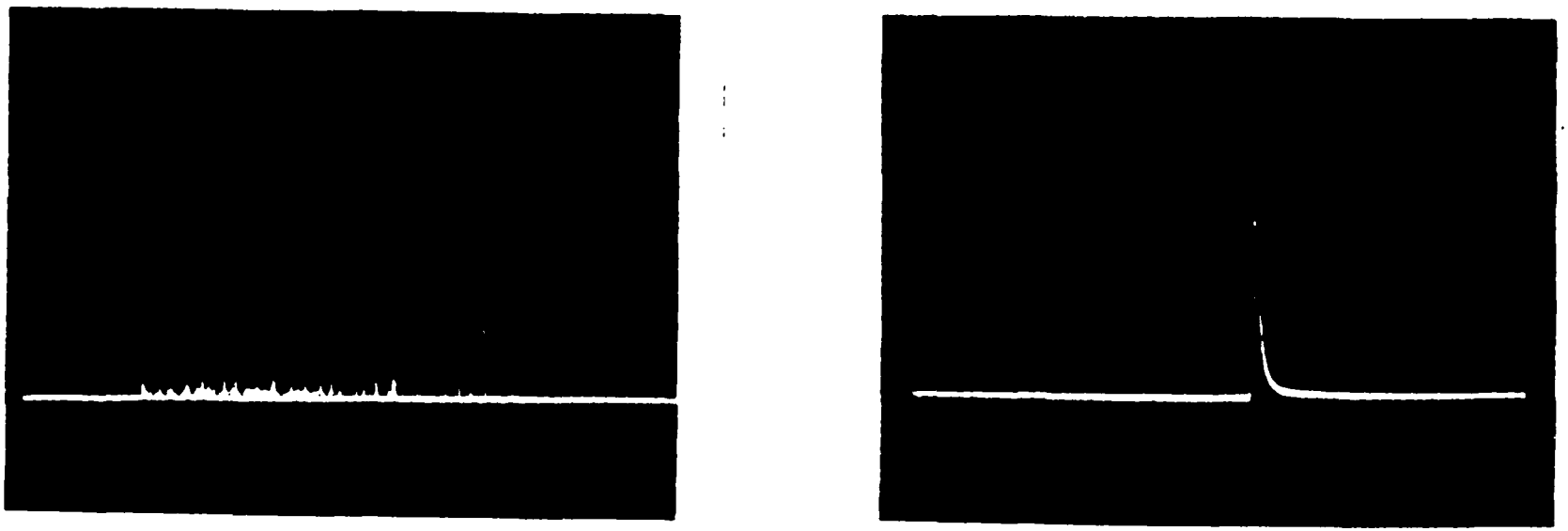

Figure 14 - Laser output as detected by a PIN diode. (A): Relaxation mode output, 0.1V, 0.2ms/div. A calorimeter measured the total output energy in this shot to be 1.7 Joules. (B): Q-switched output, 1v, 1us/div, output energy = 0.8 J.

probe was placed 20 degrees off axis and 4.3 cm from the focal spot. The results of these experiments are presented in Figure 15 and calculations yield electron temperatures of 8.7, 11.1, and 10.7 eV at 2, 5, and 10 us, respectively.

We have also looked at the ablation plasma emission spectra by replacing the Pyrex vacuum chamber with a large glass window on the target chamber and flange and focusing the light onto the entrance slit of an optical multichannel analyzer (OMCA). Spectra obtained from three separate shots are presented in Figure 16. Although we were unable to calibrate for intensities to obtain line ratios and obtain plasma temperature, these spectra show that we are producing carbon ions within a charge state of at least +2.

IIb.6) Beam/Plasma Interaction Experiments

We have measured changes occurring when energetic hydrogen particles interact with a carbon ablation plasma. Timing is such that the laser is Q-switched after the particle beam is well established. Our initial experiments exhibited a low signal to noise ratio. Further investigations identified more than one source for the interference received by the detector signal. First, it was found that the high frequency signal occurring when the laser is Q-switched was due to the detector circuit acting as an antenna, receiving the noise generated by the pockels cell circuit. Second, it was found that the EMI (electromagnetic interference) problem was aggravated by ground loops in the system. Third, it was found that the

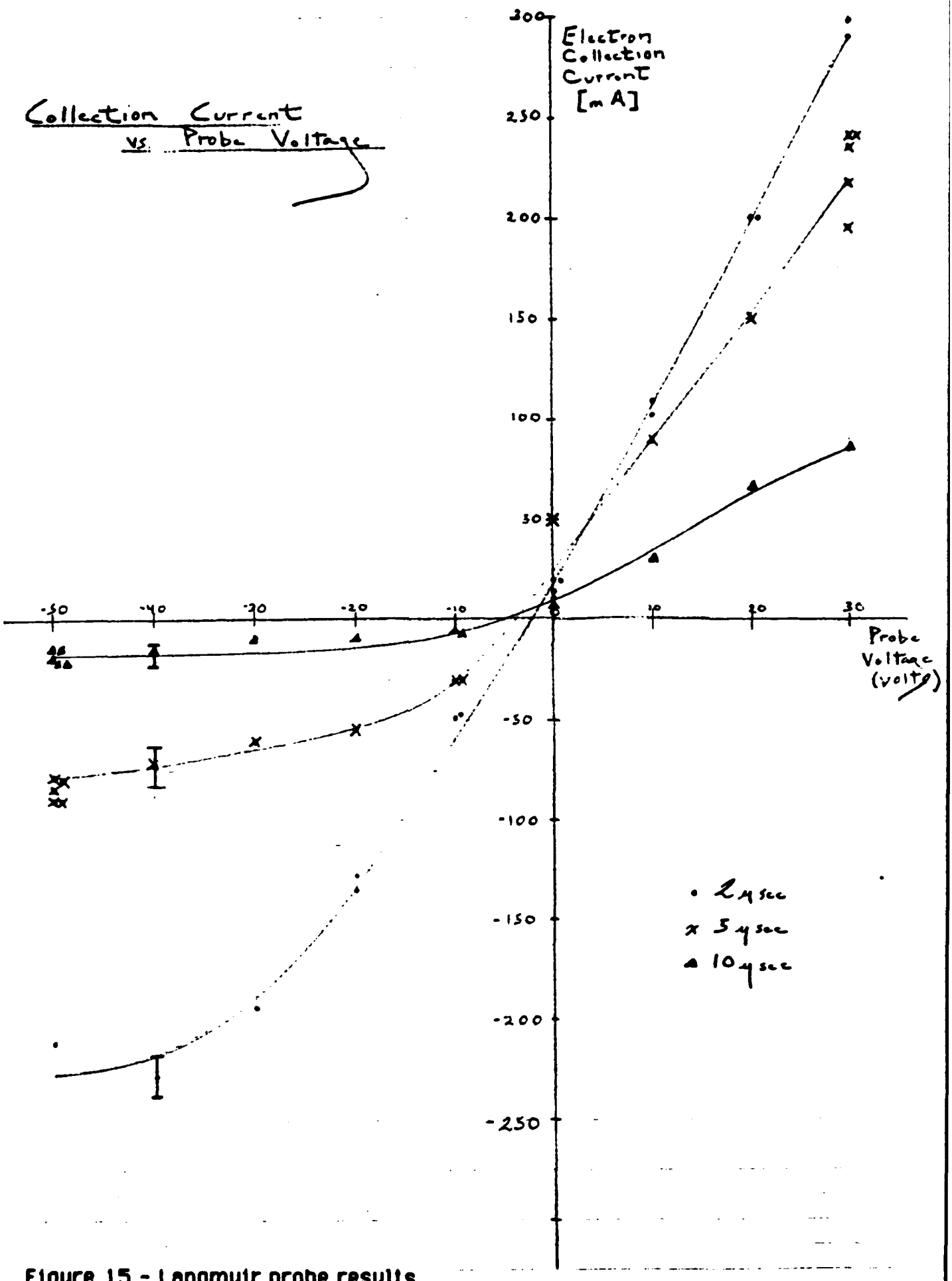

Figure 15 - Langmuir probe results.

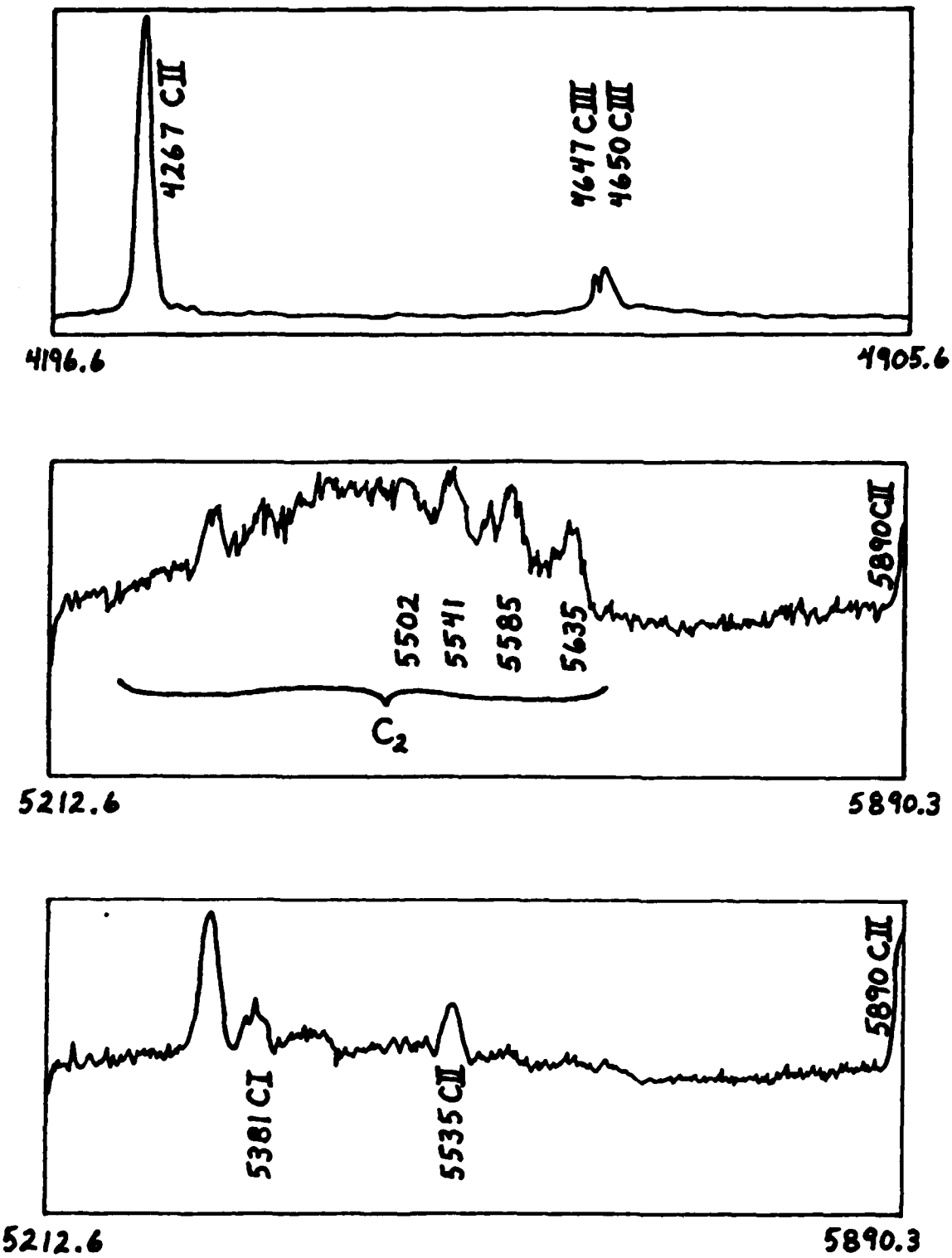

Figure 16 - Ablation plasma emission spectra. Reference 3 used for peak identification.

detector was too close to the plasma, that there was significant streaming of plasma into the detector.

Adding a second Pyrex piece to place the detector further from the target chamber helped to reduce the third source but not to eliminate it, and so small apertures were placed between the target chamber and the Pyrex system, requiring the addition of the third pumping system. Next, ground loops were eliminated and attempts were made to shield from the EMI by placing copper sheet and RF shielding tape around the pockels cell, which significantly reduced the magnitude and duration of the noise picked up by the detector circuit.

With the noise levels reduced to the point where we could make meaningful measurements of the small change in detector current following the firing of the laser, the full beam/plasma interaction experiment was conducted using 10 keV hydrogen beams and Q-switched laser pulses. Typical attenuation data for the case of no bending magnet current (neutral + ion beam) and for 18 amps of bending magnet current (neutrals only) are presented in Figure 17. It is seen that as much as 12% of the beam current is lost due to beam interactions with the plasma.

Data from a "neutrals only" shot is presented in Figure 18 along with a best fit of the self-similar expansion model. The model yields a value of the maximum line density which, for a maximum attenuation of approximately 13%, agrees quite well with the simple predictions given in Figure 2.

NEUTRAL (87%) + ION (13%) BEAM

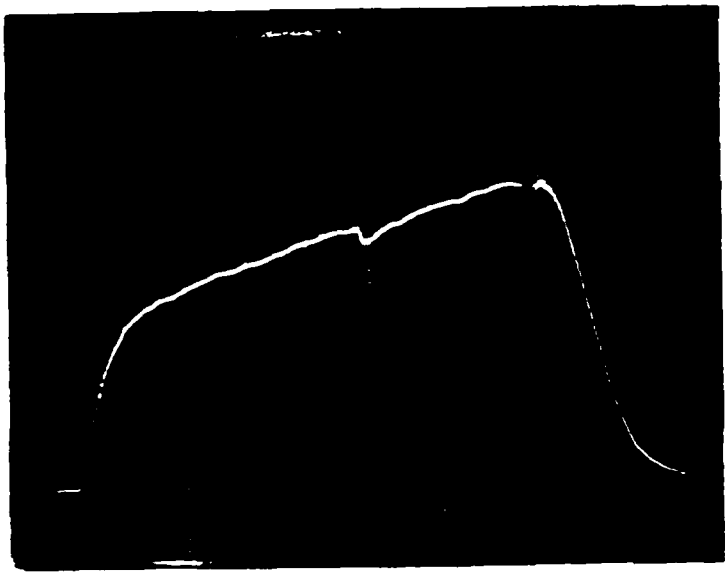

10 mV, 50 μs / div

$\left|\frac{I}{I_o}\right|_{min} = 0.94$

SHOT #1166 :

$V_{accel} = 9.8$ kV, $I_{mag} = 0$

$I_{arc} = 22$ A, $I_{drain} = 0.52$ A

$I_{detec} = 4.0\,\mu$A at t=225 μs

Beam ion fraction ~ 0.13

Laser : ~ 0.1 J on target
~ 40 ns FWHM
(~ 1×10^{12} W/cm^2 peak)

NEUTRAL BEAM (>99%)

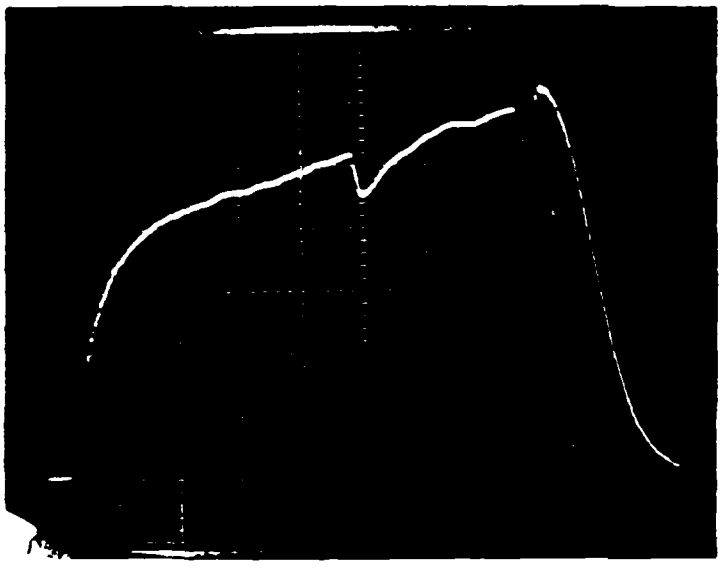

5 mV, 50 μs/div

$\left|\frac{I}{I_o}\right|_{min} = 0.88$

SHOT #1171 :

$V_{accel} = 10.0$ kV, $I_{mag} = 18$ A

$I_{arc} = 20$ A, $I_{drain} = 0.39$ A

$I_{detec} = 2.6\,\mu$A at t=225 μs

Laser : ~ 0.3 J on target
~ 40 ns FWHM
(~ 3×10^{12} W/cm^2 peak)

Figure 17 - Typical attenuation data.

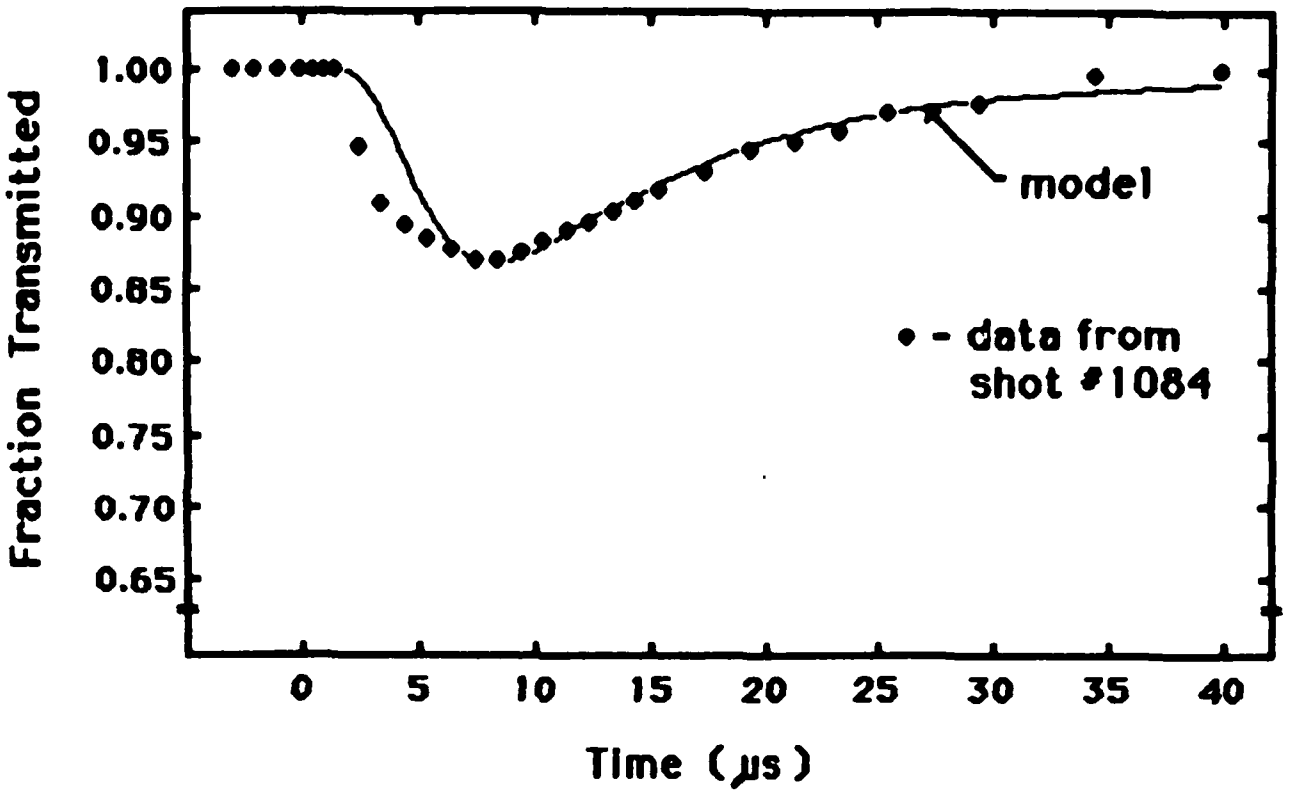

Shot #1084 : V_{accel} = 10 kV, I_{mag} = 18 A

Model : Self-similar expansion normalized to the data at the point of maximum attenuation, which yields

$$\bar{n}_{max} = 2.8 \times 10^{13}\ cm^2$$

Best fit obtained with k = 4, $v_z^\bullet = 3 \times 10^6$ cm/s

Figure 18 - Neutral beam attenuation, experiment vs. model.

Current work includes providing the means by which we can discriminate between beam ions and neutrals in order to correlate shots such as are shown in Figure 17. We are also investigating the discrepancy between data and model in the first 5 us after firing the laser, seen in Figure 18. The ion fraction with the magnetic field on is less than 1%. For the case of no bending magnet the ion/neutral fraction is estimated to be 13%:87%.

IIc) Fabrication of an Applied - B Ion Diode for the Febetron

In order to achieve higher energy and higher current ion beams for our interaction experiments we have fabricated an applied B (radial) magnetically insulated ion diode which is compatable with our existing Febetron Pulser. The higher energy beam will permit us to obtain higher energy scaling data compared to the 20 kV duopigatron data, whereas the higher beam current should improve the signal to noise ratio of our particle detectors. The Febetron parameters are:

Voltage Maximum = 500 kV

Current Maximum = 1.4 kV

Pulselength = 400 nsec. full width on current

A schematic illustration of the applied - B diode as configured for the Febetron is depicted in Figure 19. (This design is similar to those described in references 4 through 9.) The Febetron will initially be run in positive polarity with a flashboard anode and a carbon brush cathode. Figures 20 and 21 give more detailed views of the recently constructed ion diode magnet coils and vane structure. The

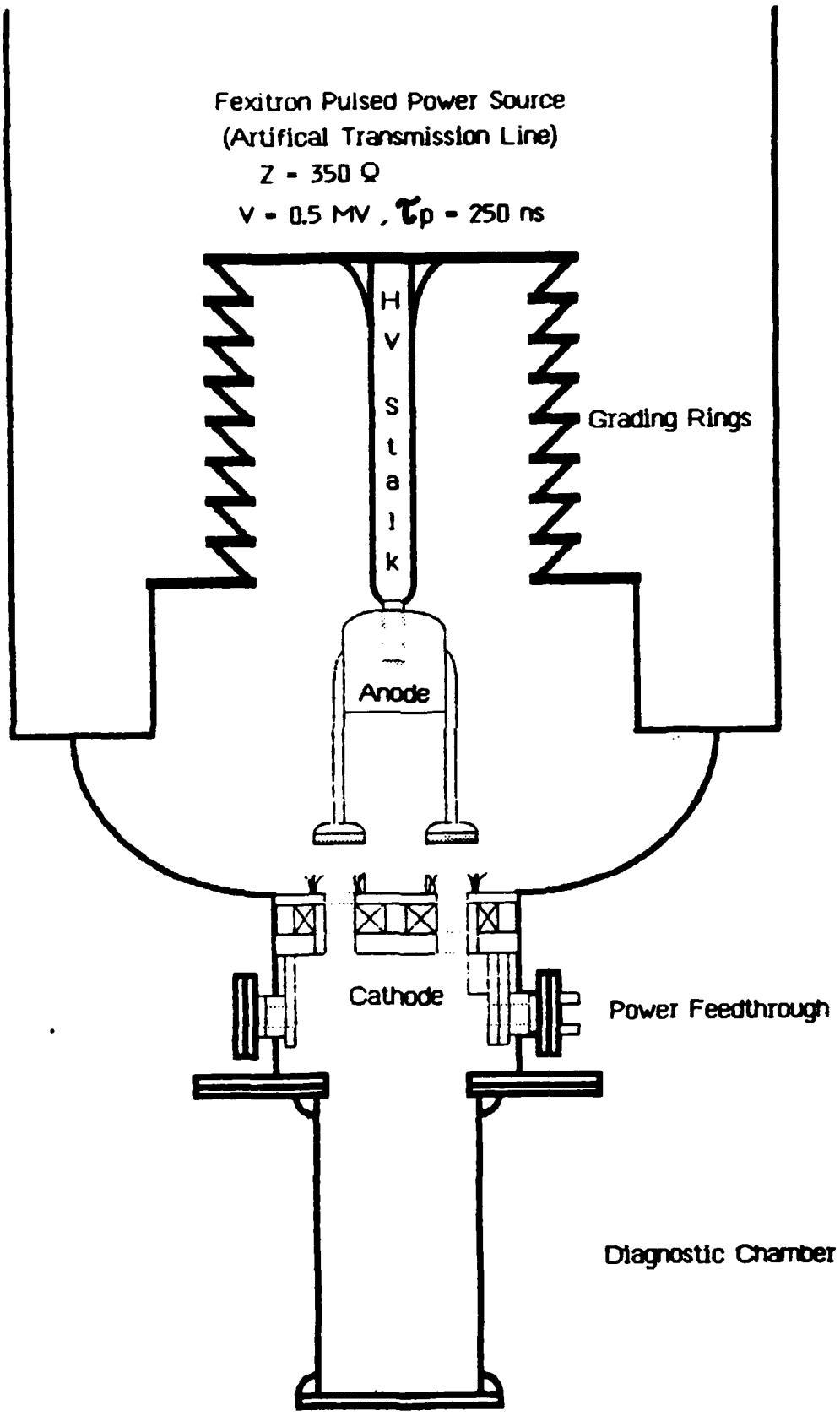

Figure 19 — Diode Experimental Assembly

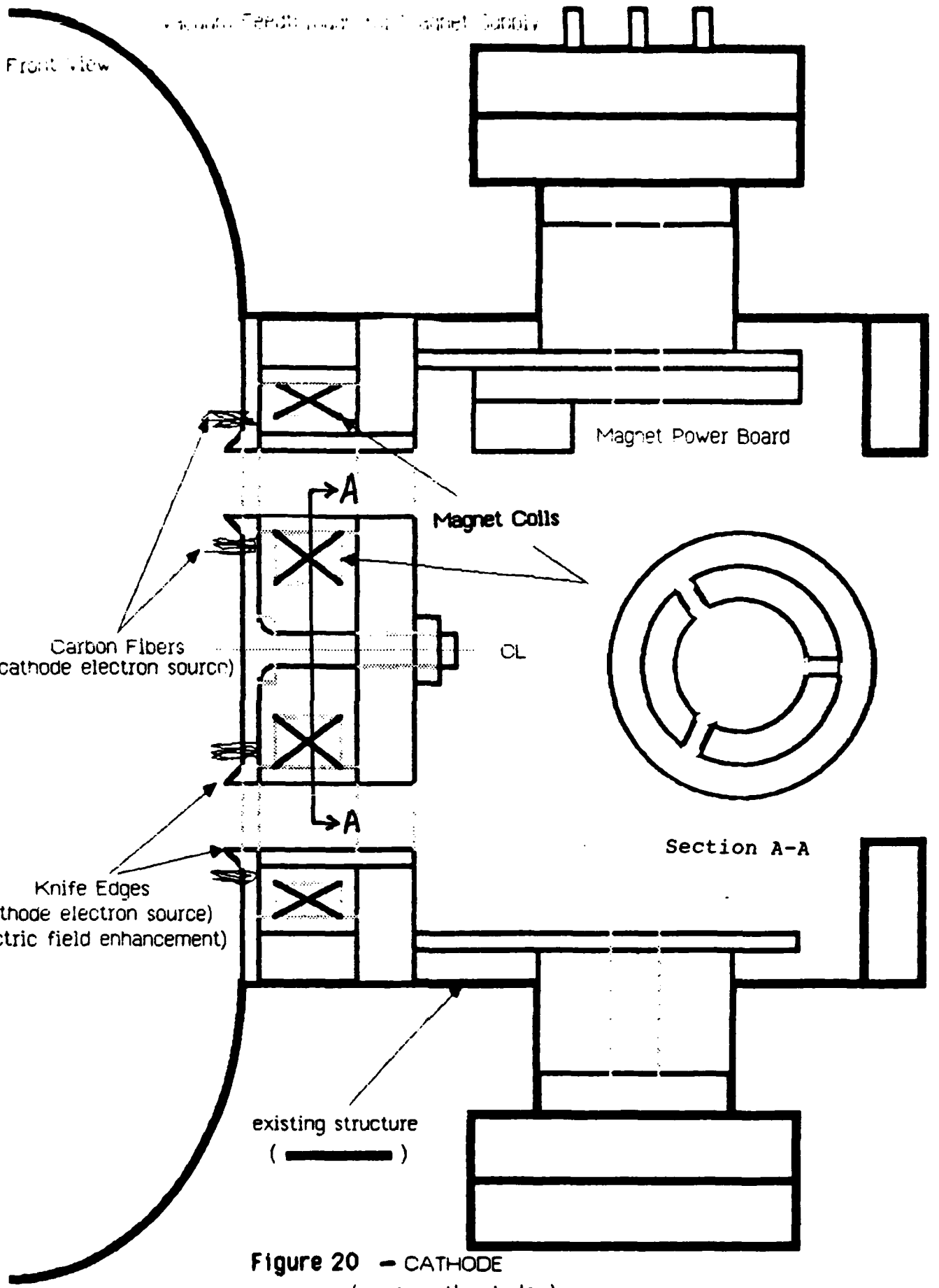

Figure 20 – CATHODE
(cross-sectional view)

Figure 21

flashboard anode (Fig. 22) employs a lucite plate with imbedded copper pins.

An important consideration in the design of this diode was the necessity of achieving a radial magnetic field which exceeds the critical insulating field. The critical insulating field for a 1-D planar diode can be calculated from the expressions given in references 10-13. Assuming that we wish to operate at 1.5 times the critical field the following table gives the required performance of our ion diode:

V(kV)	B_{crit} (Gauss)	1.5 B_{crit} (Gauss)
50	772	1158
100	1118	1677
200	1650	2475
300	2101	3152
400	2516	3775
500	2911	4366

The magnitude of these fields dictated that the magnet coils needed to be operated in the pulsed mode. The capacitive discharge magnet power supply depicted in Figure 23 was constructed for this purpose. Details of the ignitron firing circuit are given in Figure 24. Typical data for the magnet current trace and integrated B dot loop signals are given in Figure 25. The measured radial magnetic field (Figs. 26 and 27) easily exceeds the critical insulating field for the magnet and power supply which we have constructed.

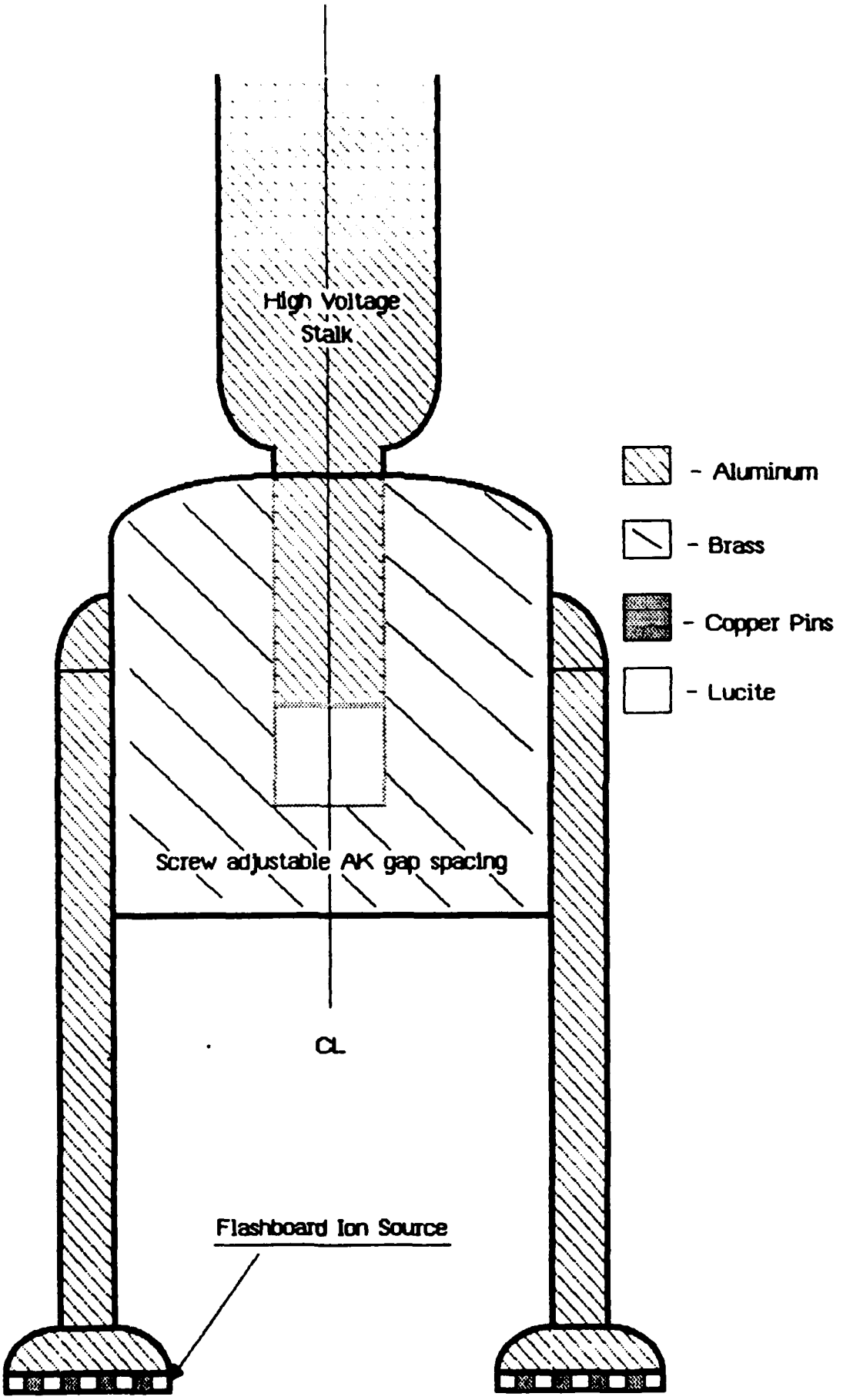

Figure 22 - ANODE
(cross-sectional view)

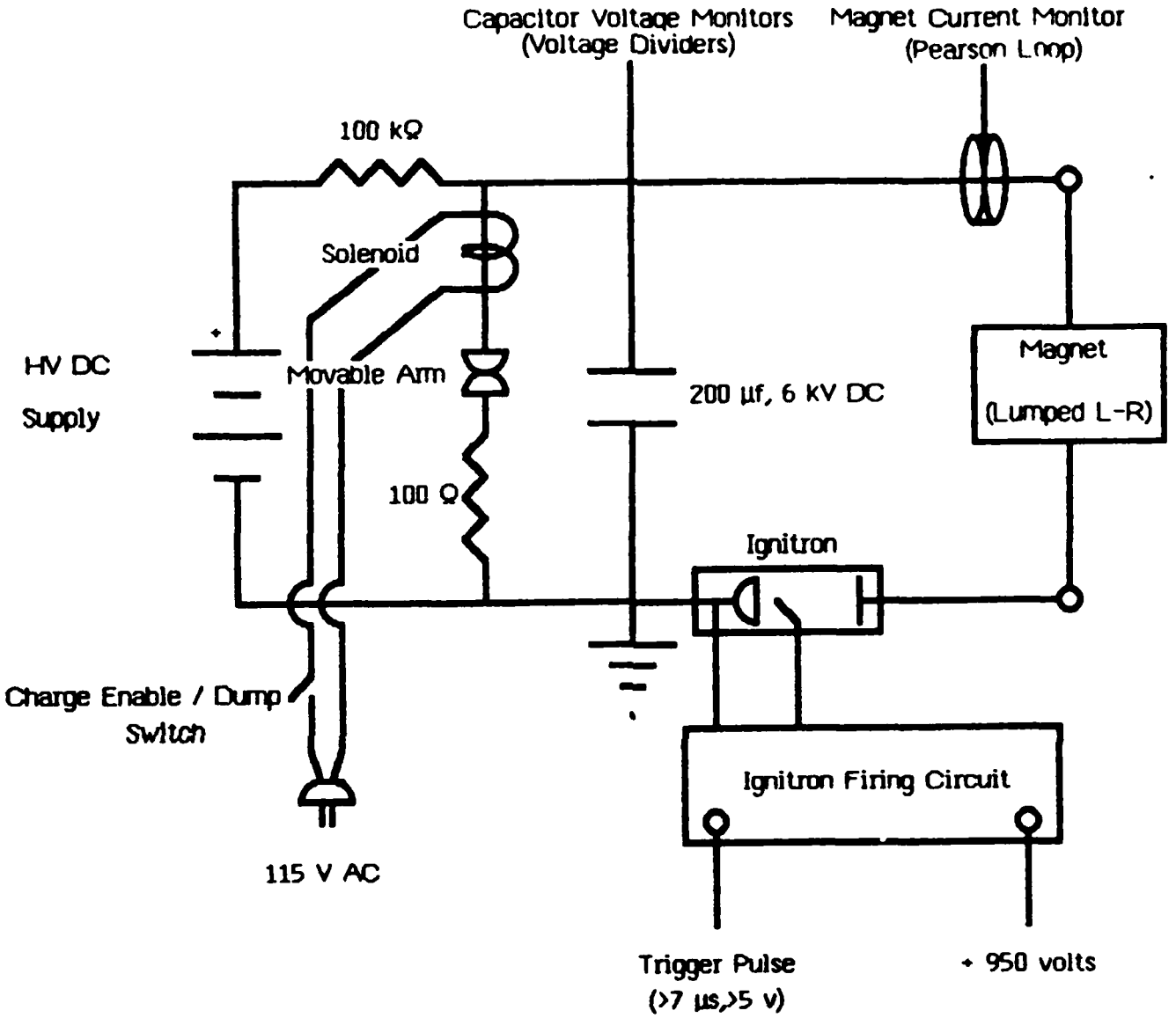

Figure 23 – Pulsed Magnet Supply

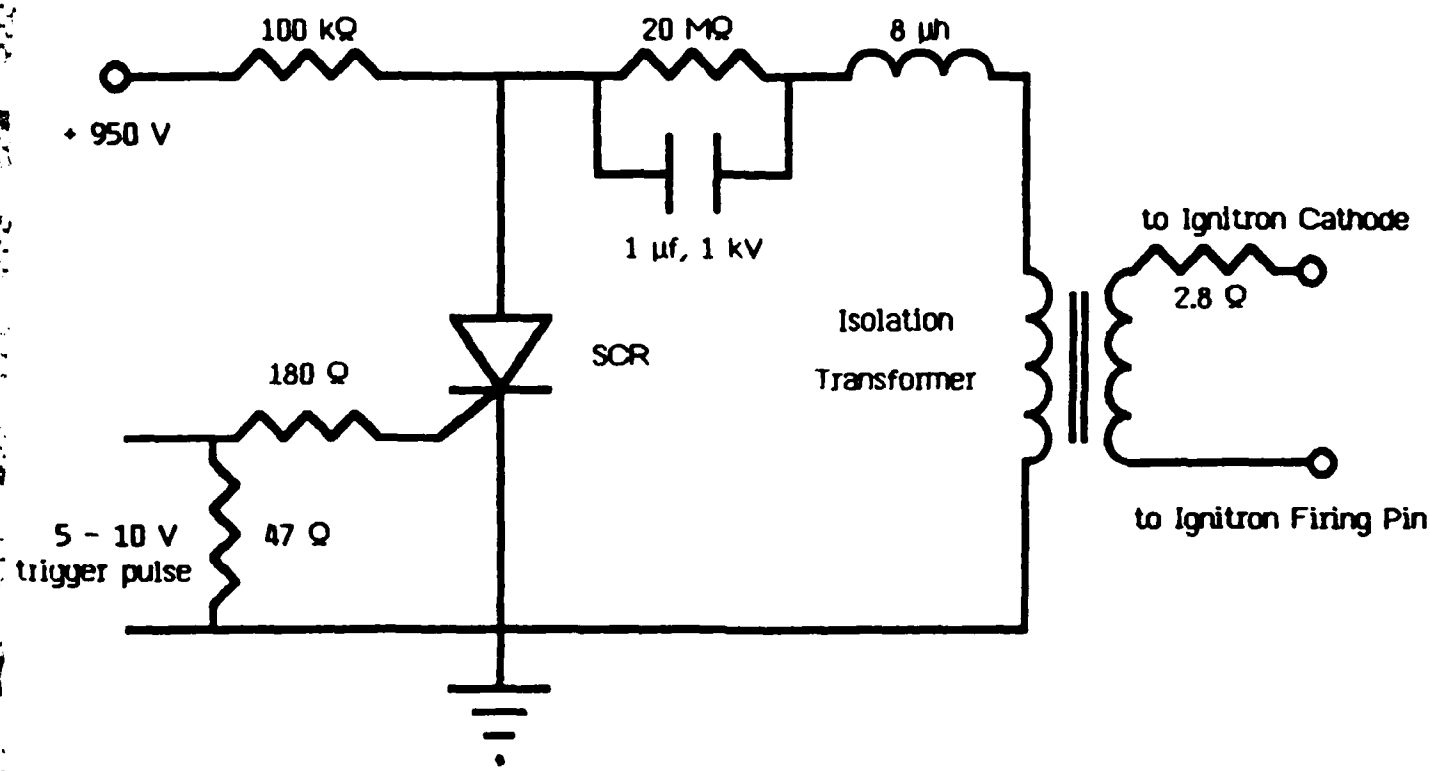

Figure 24 – Ignitron Firing Circuit

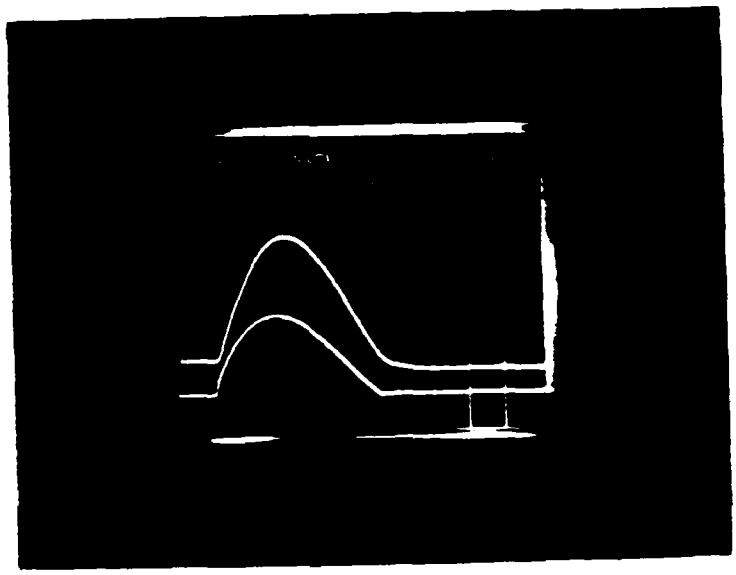

Fig.25- Top trace: example of self-integrated B dot probe (r = center of gap, z = 3.5 cm) 100 turns, A = 4.95 x $10^{-5}m^2$, RC = 22 ms, V = 2 KV Note that the trace for B(t) follows the current very well signifying good integration of the signal.

Bottom trace: Magnet current measured through Pearson coil 0.05 v/amp x 30.0 atten

AXIAL MAGNETIC FIELD VARIATION

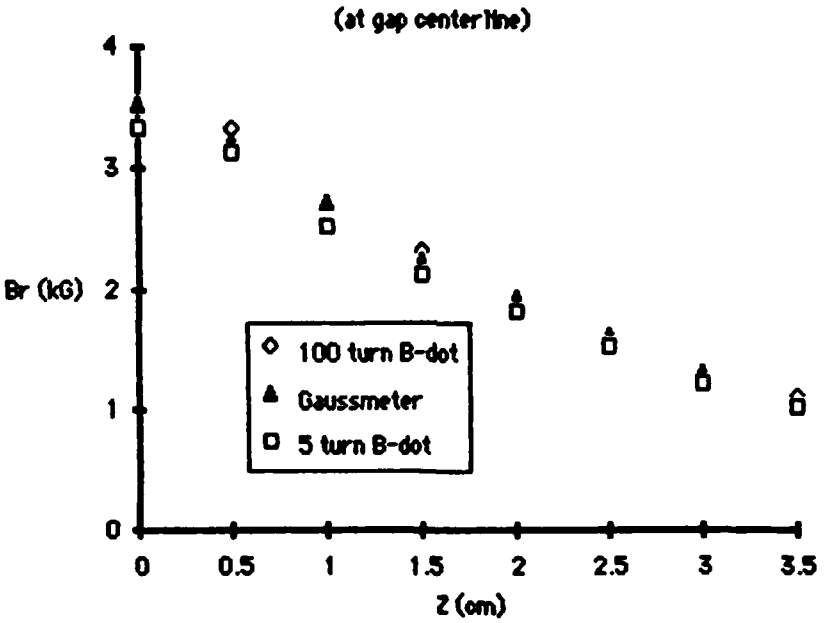

Figure 26

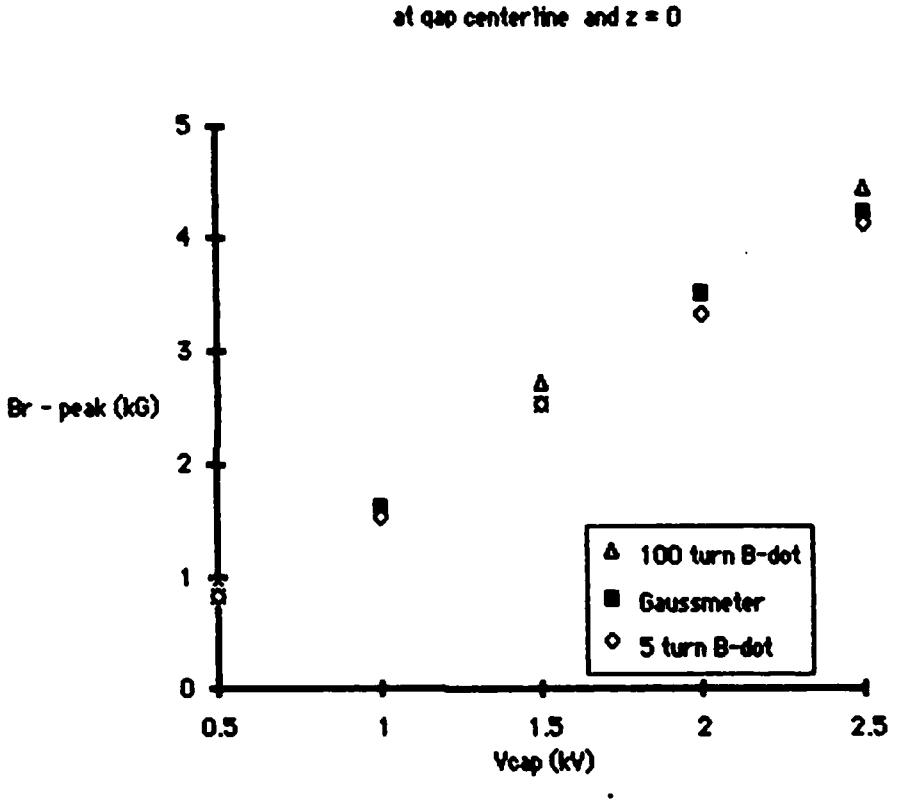
at gap centerline and z = 0
Br - peak (kG)
5
4
3
2
1
0
0.5
1
1.5
2
2.5
Vcap (kV)
100 turn B-dot
Gaussmeter
5 turn B-dot

Figure 27

REFERENCES FOR SECTION II

1. R. A. Hulse, D. E. Post and D. R. Mikkelsen, J. Phys. B 13 (1980) 3895.
2. G. J. Tallents, Laser and Particle Beams (1983), Vol. 1, Part 1, pp. 171-180.
3. Selected Tables of Atomic Spectra, NSRDS-NBS 3, Section 3, Nov. 1970.
4. S. Humphries Jr., J. Appl. Phys., 49 (1978) 501.
5. S. Humphries Jr., et al., J. Appl. Phys., 51 (1980) 1876.
6. Y. Nakagawa, Jpn. J. Appl. Phys., 22 (1983) L326.
7. K. Horioka, et al., Jpn. Jor. Appl. Phys., 23 (1984) L374.
8. J. Mizui, et al., BEAMS83, p. 151.
9. Y. Nakagawa, BEAMS83, p. 163.
10. T. J. Orzechowski and G. Bekefi, Phys. Fluids., 19 (1976).
11. R. N. Sudan and R. V. Lovelace, Phys. Rev. Lett., 31 (1973).
12. R . V. Lovelace and Edward Ott, Phys. Fluids, 17 (1974).
13. T. M. Antonsen Jr. and E. Ott, Phys. Fluids,19 (1976).

III. Graduate Students Supported in Part by this Contract

1. J. W. Thornhill, Ph.D. (Dissertation Defended, Dec.'84)
2. J. Meachum, Ph.D. Candidate (Dissertation in Progress)
3. M. Cuneo, Ph.D. Candidate
4. R. Kensek, Ph.D. Candidate (Dissertation in Progress)
5. E. Pitcher, M.S. Candidate
6. L. Smutek, M.S. Candidate
7. S. Bidwell, M.S. Candidate

IV. Publications and Dissertations since June 1, 1984 Funded by this Contract

P. D. Weber and R. M. Gilgenbach, "Intermediate and High Mass Ion Beams from a 10-cm Duopigatron," Plasma Chemistry and Plasma Processing, Vol. 4, June 1984.

J. W. Thornhill, Doctoral Dissertation: "The Hydrodynamics and Ionization Dynamics of Particle Beam Heated Carbon Ablation Plasmas."

"Neutral and Ion Beam Interactions with Laser Ablation Plasmas," J. Meachum, R. M. Gilgenbach, M. Cuneo, and E. Pitcher, Presented at the 1985 IEEE International Conference on Plasma Science, June 3-5, 1985, Pittsburgh, PA.

V. Honors and Awards

R. M. Gilgenbach received the Outstanding Young Engineer Award from the IEEE Nuclear and Plasma Sciences Society. He was presented a "Centennial Key to the Future" at the award ceremony in San Jose, CA on November 30, 1984.

END

FILMED

9-85

DTIC